DEVELOPMENT OF AUTOMATED OPERATIONAL SPACE WEATHER PIPELINE AND CME EVENT ANALYSIS USING ADITYA-L1 DATA.

M.Sc. Thesis

By:

Navanit A V

DEPARTMENT OF ASTRONOMY , ASTROPHYSICS AND SPACE ENGINEERING

INDIAN INSTITUTE OF TECHNOLOGY INDORE

May, 2025

DEVELOPMENT OF AUTOMATED OPERATIONAL SPACE WEATHER PIPELINE AND CME EVENT ANALYSIS USING ADITYA-L1 DATA

M.Sc. THESIS

Submitted in partial fulfilment of the
requirements for the award of the degree
of
Master of Science

by

Navanit A V

DEPARTMENT OF ASTRONOMY , ASTROPHYSICS AND SPACE ENGINEERING

INDIAN INSTITUTE OF TECHNOLOGY INDORE

May, 2025

INDIAN INSTITUTE OF TECHNOLOGY INDORE

CANDIDATE'S DECLARATION

I hereby certify that the work which is being presented in the thesis entitled **"Development of Automated Operational Space weather Pipeline & CME event analysis using Aditya L1 data"** in the partial fulfillment of the requirements for the award of the degree of **MASTER OF SCIENCE** and submitted in the **DEPARTMENT OF ASTRONOMY ASTROPHYSICS AND SPACE ENGINEERING, Indian Institute of Technology Indore**, is an authentic record of my own work carried out during the time period from **July 2023** to **May 2025** under the supervision of **Dr. Bhargav Vaidya, Associate Professor, Department of Astronomy, Astrophysics And Space Engineering**.

The matter presented in this thesis has not been submitted by me for the award of any other degree of this or any other institute.

10/05/2025

Navanit A V
Signature of the student with date

This is to certify that the above statement made by the candidate is correct to the best of my/our knowledge.

Signature of the Supervisor of
M.Sc. thesis (with date)
(Dr. Bhargav Vaidya)

Navanit A.V. has successfully given his/her M.Sc. Oral Examination held on **05/05/2025**.

Signature(s) of Supervisor(s) of MSc thesis
Date: 10/05/2025

Programme Coordinator, M.Sc.
Date: 19/05/2025

Convenor, DPGC
Date: 19/05/2025

HoD, DAASE
Date:

Acknowledgement

First and foremost, I would like to express my deepest gratitude to my supervisor, Dr. Bhargav Vaidya, for his invaluable guidance, constant support, and insightful feedback throughout the course of my research. I extend my sincere thanks to the faculty members and staff of the Department of Astronomy, Astrophysics, and Space Engineering at IIT Indore, for providing valuable guidance, a stimulating academic environment, and the necessary resources to carry out my work. I would also like to express my sincere gratitude to my lab colleagues —Sirsha Nandy, Jithu Athalathil, Adithya Sharma, Harshitha Bhuyan, Devesh Sharma, Aryan Bhake, and Harsh Kararwal without whom this work would not have been possible. I am especially grateful to Jithu Athalathil for his significant contributions to my work. His guidance, insights, and the opportunity to learn from him have had a profound impact on my research. I am equally thankful to my batchmates — Harikrishnan, Gitaj, Anushka, Annie, Daisy, Prasad, Parth, Vishruth, Ashuthosh, Vijay, and Amar Deep for their support, collaboration, and engaging discussions that enriched my academic experience. I would also like to thank my friends – Nasmi S Anand, Leon Noble, Parvathy Thankachi , Shraddha Mohnnai, Swaroop Zachariah and Riddhi srivastava along with several others for their constant encouragement and unwavering belief in me, especially during challenging times. Their presence made this journey not only manageable but truly meaningful. A heartfelt thank you to my family for their unwavering love, patience, and support throughout this entire period. Their belief in me kept me going through the most challenging times. Finally thank you to IIT Indore for this beautiful journey, which has deepened my curiosity, strengthened my passion, and instilled in me a quiet confidence to continue exploring the wonders of science, gifting me the enduring belief to chase my dreams without hesitation or self-doubt.

Abstract

This thesis explores a critical area in space weather research: the design and development of an Automated Space Weather Framework. Solar wind and coronal mass ejections (CMEs) are fundamental drivers of space weather, and effective prediction and mitigation depend on precise, automated, and operational forecasting of these phenomena. The aim of this work is to develop a fully operational, end-to-end, automated space weather forecasting system for the SWASTi framework. Space Weather Adaptive Simulation(SWASTi) is a numerical framework for simulating ambient solar wind and CME. The automated architecture enables the integration of various space weather modules such as Solar wind Module, CME module, and others into a cohesive tool providing space weather modeling. The system deployed on a compute cluster enables seamless interaction and remote operations of the automated level architecture to create advanced modeling that simulates processes from the Sun to Earth or any other user-specified vantage point. Visualization tools are implemented as modular components that can seamlessly integrate with any preinstalled simulation or forecasting module in the system, provided their outputs are compatible. This design ensures efficient data interaction and analysis. The automated system allows users to interact through a front end, where they can run complex, coupled simulations and view, retrieve, and visualize output data. This setup also enables model output validation and comparison, providing a robust platform for operational space weather forecasting.

Contents

References

List of Figures

List of Tables

Chapter 1

Introduction

Space weather refers to the dynamic changes in the space environment, driven primarily by solar activity. The solar activity of the Sun follows a cyclic variation, resulting in observable changes on the Sun's surface and space environments. This causes continuous cycles of magnetic variations, creating transient phenomena like Coronal mass ejection (CME), solar flares, and solar wind that originate from the Sun and propagate outward, interacting with the planetary atmosphere and magnetic fields across the solar system. These geomagnetic disturbances occurring within the interplanetary medium are what we refer to as space weather.

The fundamental principles behind space weather phenomena lie in solar plasma physics. Plasma is an ionized gas of charged particles and is the most abundant state of matter in the universe. We know that coronal holes and active regions in the Sun are areas of open magnetic field lines, allowing solar plasma and energized particles to stream outward into the solar system. These are solar flares, coronal mass ejections (CMEs), solar energetic particles (SEPs), and solar wind which are the primary drivers causing space weather phenomena. These massive structures form within minutes as clouds of magnetized plasma propagate into interplanetary space. The most intense geomagnetic storms are typically triggered by rapid large-scale CMEs, which drive large-density waves. Coronal Mass Ejections (CMEs) eject immense amounts of plasma from the Sun's corona, transporting magnetic fields that are embedded within the outflow. These fields are considerably stronger than the interplanetary magnetic field (IMF) typically present in the background solar wind. CME speeds can range from several kilometers per second to almost 3000 kilometers per second (Gopalswamy [2004]). The speed of propagation is very important because high-speed CME can cause huge impacts. The initiation of a CME begins with the magnetic reconnection occurring in the Sun's corona. Magnetic reconnection is a process in which oppositely directed magnetic field lines within a plasma break apart and merge, releasing energy in the process. The CME gains additional energy

through the release of stored magnetic energy during the process of reconnection.

After the magnetic reconnection, the plasma will burst into interplanetary space and accelerate particles to high energy causing the solar flare. Solar flare is an energetic fast process. The electromagnetic radiation released in minutes will vary from radio wavelength to X rays even gamma rays. Flares are classified into different classes. X-class flares are the most intense, followed in strength by M, C, and B-class flares, with A-class flares being the weakest. The probability of a X class flare to come along with a CME is very high (Yashiro et al. [2006]). During the high energy event, the accelerated particles are known as solar energetic particles (SEP). The energy of the SEPs reaches from a few keV of supra-thermal particles to some GeV. SEP events are detected in situ as increased fluxes of electrons, protons, and heavy ions. M class flare can lead to minor radiation and temporary radio blackouts, especially over polar regions (Echer et al. [2005]). The high energy SEP in the range of GeV or an X class flare is the major reason for the spacecraft charging and also can produce ground level enhancement (GLE), which can cause some radiation exposure on crewed spacecraft (Malandraki and Crosby [2018]).

The solar wind is a continuous flow of particles emitted from the Sun's atmosphere, carrying the Solar magnetic field with it. The solar wind is a key factor in structuring interplanetary space because Solar wind acts as an ambient environment that affects the movement of space weather drivers throughout the heliosphere. Slow wind streams and fast wind streams interact to create Stream Interaction Regions (SIRs), which are also considered major drivers of space weather. The slow solar wind originates mainly from equatorial latitudes of the Sun, having an average velocity of up to 400 kms^{-1}. The fast solar wind originates on the poles and has velocities up to 1000 kms^{-1}.

To develop a complete understanding of space weather we need to consider all the above primary drivers originating from the Sun's active region and coronal holes. The number of active regions and coronal holes are related to solar activity. Because of the internal dynamo effect, solar activity is a cycle of 11 years. The solar cycle has minimums and maximums. At solar minimum, the number of sunspots is less, and coronal holes are primarily found at the poles. While at solar maximum magnetic activity is at its peak, Coronal holes occur more frequently and also at the equator which increases the transient events like CME and flares. The "Carrington event" on September 1 1859, an extreme geomagnetic storm, stands as a historical example of extreme space weather. This event serves as a reminder of the societal risk posed by space weather, including the disruptions of satellite communication, GPS systems, power grids, and other critical infrastructure.

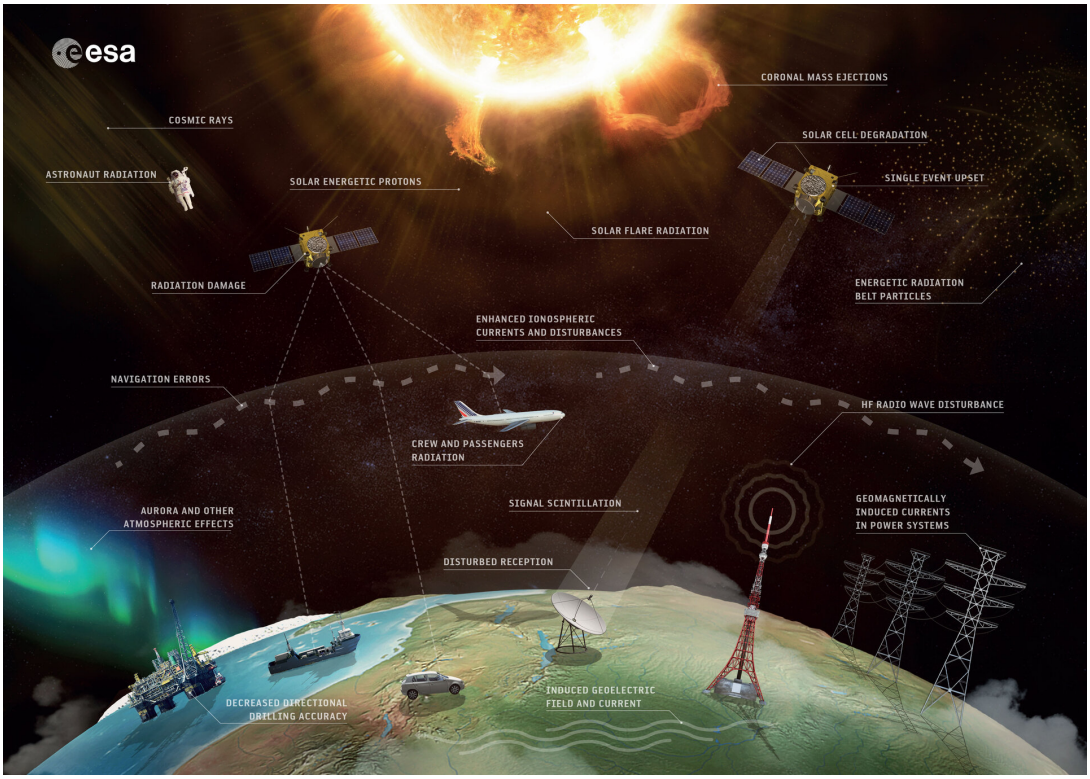

Figure 1.1: This image illustrates the impacts of space weather on Earth and in space. The effects depicted range from satellite and communication disruptions, including signal scintillation and disturbed reception, to increased radiation exposure for astronauts and airline passengers. Space weather also affects terrestrial systems, with geomagnetically induced currents damaging power grids, navigation errors, and disturbances in global positioning systems (GPS). Image Credit: ESA

This project focuses on developing an automated space weather prediction system for the SWASTi framework, a numerical system for simulating the solar wind and Coronal Mass Ejections (CMEs) (Mayank et al. [2022, 2023]). Swasti framework uses a two-layer setup of a coronal layer and heliospheric MHD simulation layer. However, these models are often complex, making them challenging to install and operate effectively. The Community Coordinated Modeling Center (CCMC) is a collaborative initiative supported by multiple agencies, including NASA and the National Science Foundation (NSF). Its mission is to facilitate, support, and advance research and development efforts focused on space weather forecasting. There are a few models available such as the Space Weather Modeling Framework (SWMF) Tóth et al. [2005] developed at the University of Michigan's Center for Space Environment Modeling (CSEM), which integrates multiple simulation modules into a single environment. Additionally, established models like EUHFORIA (Pomoell and Poedts [2018]), ENLIL (Odstrcil [2003]), and SUSANOO (Shiota et al. [2014]). The proposed system incorporates an architecture that automates the entire simulation and forecasting pipeline, leveraging containerization techniques to streamline the coronal and inner heliospheric model modules in SWASTi framework. This system

integrates real-time data from magnetograms, such as GONG, or ADAPT, as inputs, ensuring continuous and efficient operation. The PLUTO code (Mignone et al. [2007]), a numerical tool based on the Godunov scheme for solving conservation laws, is employed for automating the inner heliospheric model. This automated and operational Framework enhances the efficiency and user performance through the friendly user interface of the fully automated SWASTi simulation, making space weather forecasting and research more faster and accessible.

1.1 Objective and Motivation

The objective of this project is to design and implement an automated operational space weather prediction. The system aims to streamline the simulation and forecasting of solar wind and CMEs, integrating advanced numerical models. Key goals include:

- Design and Develop a fully operational and automated architecture for the easy simulation of solar wind and CME.
- Integrating daily magnetogram data inputs (GONG, ADAPT) seamlessly into the simulation pipeline for daily simulations.
- Creating a backend to carry the simulation for the autonomous system and combining it with a user-friendly frontend for the easiness of handling our model.
- CME event analysis conducted using the automated pipeline, with comparative evaluation against observational data from Aditya-L1.

The motivation for this project stems from the increasing significance of space weather forecasting in an age of rapid space exploration and growing dependence on satellite technologies. Developing an automated system for space weather modeling offers an efficient solution to support future space missions. Moreover, such systems will enable a more comprehensive analysis of space weather from multiple vantage points, improving forecasting accuracy and responsiveness.

Chapter 2

SWASTi Framework & Setup

The first chapter covered all the key topics in solar physics that cause space weather. We have clearly explained the configuration of the Sun's magnetic field below the photosphere which is the core cause of space weather phenomena. As we cannot directly observe the magnetic changes happening, it is challenging to predict its dynamics with certainty and limitations in observing the photosphere magnetic fields of the Sun, particularly for the space weather simulation. It necessitates the use of a simulation framework including MHD models to support our understanding and forecasting capabilities. In this chapter, we introduce the SWASTi framework for simulating solar wind and CMEs, encompassing both coronal and heliospheric models. SWASTi is the numerical simulation framework that I am using for the development of this automated space weather system. we will explore the details of the Framework, workflow, submodules, and the step-by-step processes involved in SWASTi's functioning.

2.1 SWASTi: Space Weather Adaptive SimulaTion Framework

The Space Weather Adaptive SimulaTion (SWASTi) framework is a numerical framework for forecasting and simulating the ambient solar wind and CME. SWASTi is composed of two distinct models: one dedicated to simulating the solar wind (SWASTi-SW) and the other focused on CMEs (SWASTi-CME). For CME, this framework includes a nonmagnetized elliptic cone model and a magnetized flux rope CME model which I will explain in this chapter later. SWASTi employs a framework that integrates a semiempirical coronal model with a physics-driven inner heliospheric model. This approach provides capabilities comparable to well-established models like ENLIL, SUSANOO, and EUHFORIA.

The coronal model domain extends from 1.0 $R_\odot$ to 21.5 $R_\odot$, equivalent to 0.1 AU,

while the inner heliosphere model covers from 0.1 AU to 2.1 AU. The main role of the coronal model is to supply the outer boundary conditions for the inner heliospheric model, with a radial boundary R_{in} at the location where the solar wind transitions to supersonic and super Alfvenic (Goelzer et al. [2014]) set at $21.5R_{\odot}$. The Inner Heliosphere model then receives these boundary conditions from the coronal model and computes the solar wind's physical properties, such as density, velocity, and temperature, as it propagates outward.

SWASTi utilizes a synoptic magnetogram as its inputs and is built with a modular design that enables coupling of the Potential Field Source Surface (Altschuler and Newkirk [1969]) model with the Schatten Current Sheet (SCS), Schatten [1971] model. This approach allows for configurations using either the PFSS model alone or the PFSS+SCS combination. Both configurations utilize the empirical WSA model (Arge et al. [2003])to derive the solar wind speed profile at the inner boundary, R_{in}. Figure 1 provides a summary of the SWASTi framework's process flow, showcasing the progression from magnetogram input to the calculation of plasma characteristics in the inner heliosphere. The key terms and concepts introduced will be explained in detail in the upcoming sections.

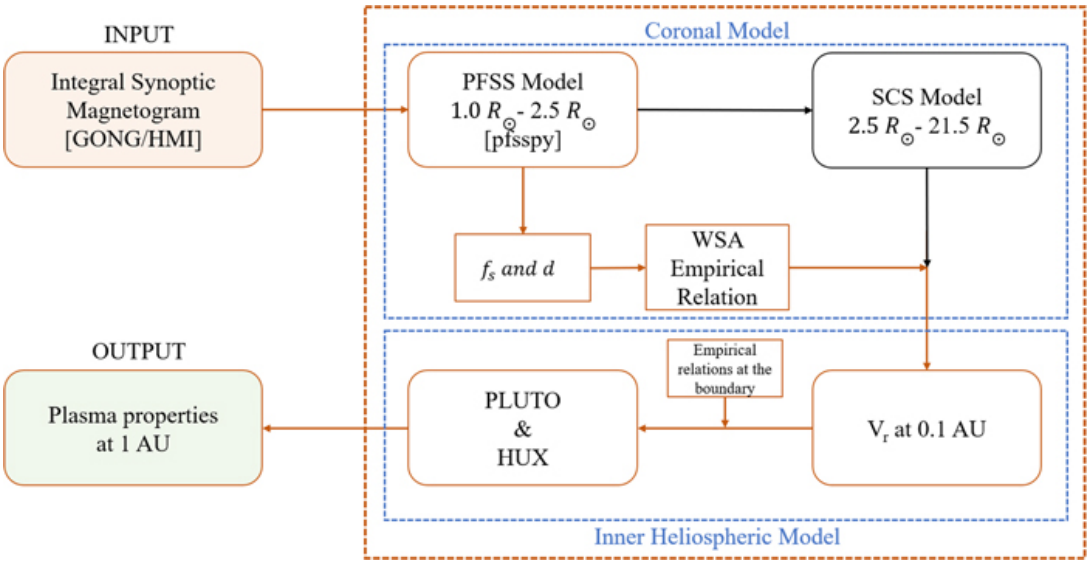

Figure 2.1: Workflow of SWASTi solar wind model, illustrating the models within each subdomain and their workflow. (Image Credit: Mayank et al. [2022])

2.1.1 Coronal Model

The coronal model is responsible for deriving the inner boundary conditions for the inner heliospheric model. It utilizes a semiempirical coronal model that contains the Potential Field Source Surface (PFSS) model, Schatten Current Sheet (SCS) model, and empirical WSA model.

Input Magnetogram

The sole input for the coronal model is a full-disk magnetogram of the photosphere, which gives the magnetic field data from the solar surface. For this work, we have utilized integral Carrington rotation (CR) synoptic maps from GONG-ADAPT and NSO-GONG for this work. CR synoptic magnetograms are used because each point on the longitude corresponds to the earth's position during that specific Carrington rotation period. This approach enables the streamlined generation of inputs for analyzing ambient solar wind propagation effectively.

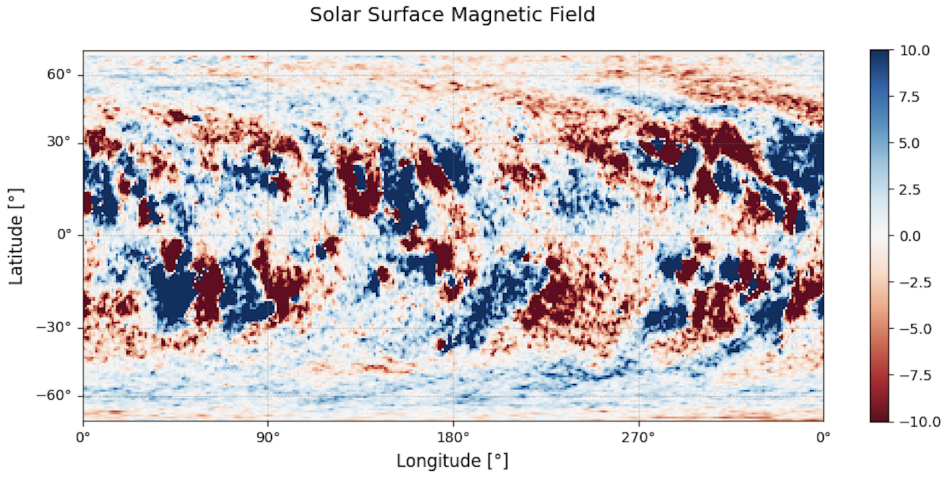

Figure 2.2: synoptic magnetogram from GONG for CR 2280

PFSS Model

The PFSS model is used to calculate the global magnetic field in the lower solar corona. It enables the tracing of magnetic field lines and provides insights into the locations of coronal holes and open magnetic field regions. PFSSPY (Stansby et al. [2020]) is used to do this. PFSSPY is a Python-based finite-difference solver designed for implementing Potential Field Source Surface (PFSS) modeling. SWASTi utilizes $100 \times 181 \times 361$ resolution for the grid to compute the magnetic field lines from $1R_{\odot}$ up to the source surface radius (R_{ss}), which is 2.5 $R_{\odot}$.

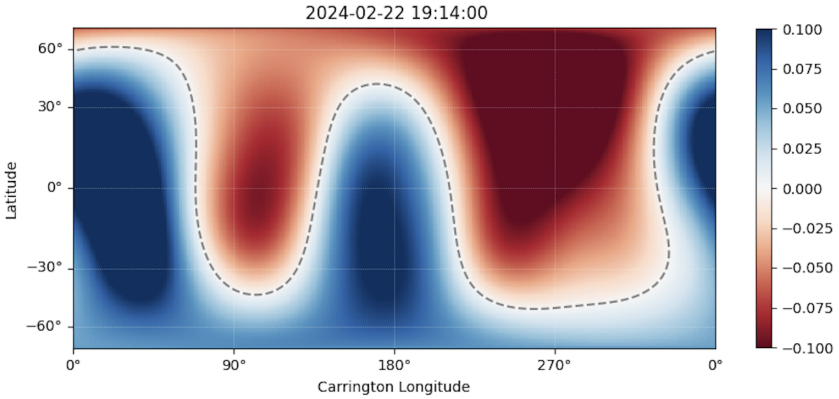

Figure 2.3: Magnetic flux density obtained from PFSS at source surface.The blue line represents the polarity inversion.

The magnetic field line tracing is performed in two stages: initially, from the inner boundary at 1 $R_\odot$ to the outer boundary at 2.5 $R_\odot$, capturing both open and closed field lines that define the perimeter of the coronal hole. In the second stage, field lines are traced from the source surface back to the solar surface. However, the method considers only the open magnetic lines originating from coronal holes. This two-step tracing method allows for more detailed mapping of the magnetic lines at the source boundary.

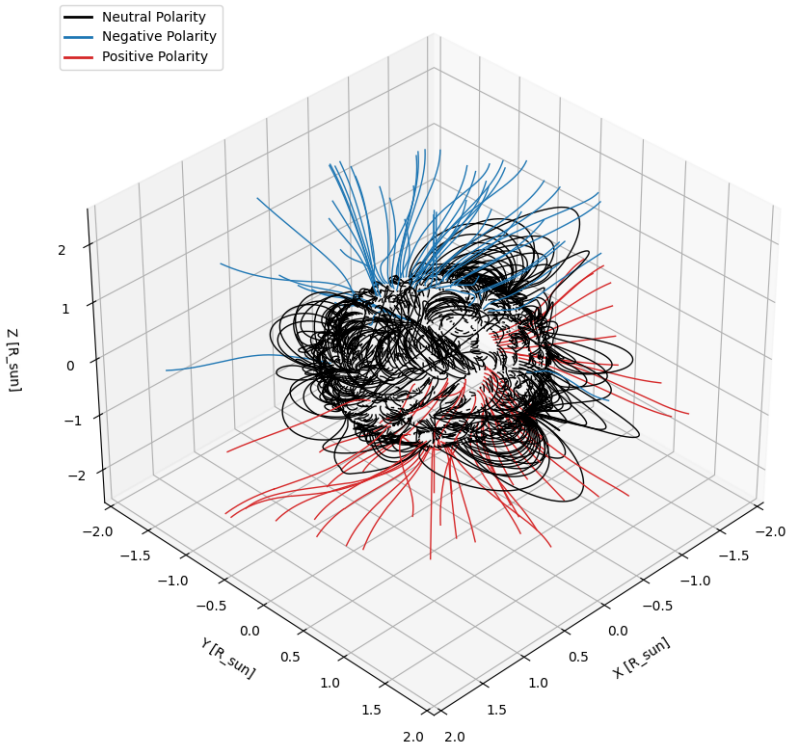

Figure 2.4: Magnetic field structure obtained from PFSS

Thus, utilizing PFSSPY to solve the global magnetic field allows us to obtain f_s and d. f_s is the areal expansion factor of the flux tube and d is the minimum angular separation of the footpoints from the coronal hole boundary.

W S A Model

The WSA (Wang-Sheeley-Arge) model (Arge et al. [2003]) is used to estimate the solar wind speed profile at the inner boundary of the heliosphere. In SWASTi the following WSA relation is used.

$$\boldsymbol{V_{R_{\text{in}}}} = \boldsymbol{V}_{\text{min}} + \frac{\boldsymbol{V}_{\text{max}}}{(1+\boldsymbol{f_s})^{\frac{2}{9}}} \times \left[\left(1.0 - 0.8 \exp\left(- \left(\frac{\boldsymbol{d}}{\boldsymbol{w}} \right)^{\boldsymbol{\beta}} \right) \right)^{3} \right] \text{km s}^{-1} \tag{2.1}$$

$$\boldsymbol{f_s} = \frac{\boldsymbol{R}_{\odot}^2 \times \boldsymbol{B}_r(\boldsymbol{R}_{\odot}, \boldsymbol{\theta}, \boldsymbol{\phi})}{\boldsymbol{R}_{ss}^2 \times \boldsymbol{B}_r(\boldsymbol{R}_{ss}, \boldsymbol{\theta}, \boldsymbol{\phi})} \tag{2.2}$$

In the equation 2.1 V_{min}, V_{max}, β, and w are independent parameters, and f_s and d we got by solving the magnetic field provided by the input magnetogram. And equation 2.2 is similar to Equation (2) of McGregor et al. [2011]. V_{min} and V_{max} are the minimum and maximum value of $V_{R_{in}}$. In the SWASTi we have fixed V_{min} and V_{max} as 250 kms^{-1} and 750 kms^{-1} respectively. The parameters w and d govern the width and position of this boundary layer. Specifically, w defines where the speed begins to rise, while d determines its position. β controls the effect of d on the solar wind speed $V_{R_{in}}$. These free parameters will be tuned for better solar wind prediction at 0.1 AU. This is a crucial step in building the database for the automated space weather system. Further details on this process will be explained in Chapter 3. The parameters f_s and d exhibit a strong correlation, with each capable of independently providing reasonable solar wind speed predictions, particularly near solar minimum. When flux tubes emerge near the boundary of an open flux region (i.e., small d), the solar wind speed tends to the minimum value V_0 regardless of f_s. On the other hand, when flux tubes are positioned far from the open or closed flux boundary (large d), the wind velocity reaches an asymptotic value determined only by f_s. These two key observations: as d increases, indicating field lines near the coronal hole's edge, the wind speed remains relatively constant and independent of f_s, and once d reaches a certain threshold, wind speed is solely dependent on f_s. This can be understood from Figure 2.5 depicts the relation of wind speed with f_s and d.

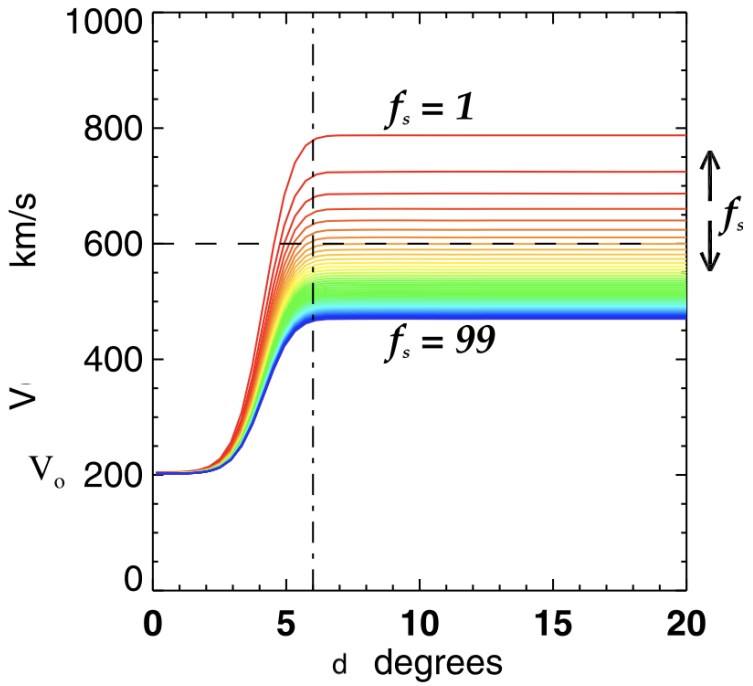

Figure 2.5: Plot of solar wind velocity versus the flux tube's areal expansion factor and the minimum angular separation of its footpoints. (Image Credit: McGregor et al. [2011])

To properly adjust the free parameters in the WSA model for better working, the empirical formula must depend on both d and f_s. So by analyzing the variation of $V_{R_{in}}$ considering the dependency of f_s and d, the value of β is chosen to be between 0.75 to 1.75.

Extrapolation to 1 AU

The velocity obtained at 0.1 AU using the WSA model is extrapolated to the L1 point using HUX model. HUX model is a 1D upwind extrapolation numerical scheme that ignores magnetic field, pressure, and gravity. HUX provides a precise representation of solar wind speed at 1 AU, (Riley and Issan [2021]). This technique requires computationally very little time. The movement of the solar wind can be characterized using the fluid momentum equation expressed in a corotating reference frame as:

$$\boldsymbol{\rho}\left(\Omega_{\text{rot}}\frac{\boldsymbol{\partial}\mathbf{v}}{\boldsymbol{\partial\phi}}+\mathbf{v}\cdot\boldsymbol{\nabla}\mathbf{v}\right)=-\boldsymbol{\nabla p}+\frac{\boldsymbol{GM_s}}{\boldsymbol{r}^2}\boldsymbol{e}_r \tag{2.3}$$

This momentum equation simplifies to Non viscous Burgers's equation while ignoring the influence of the magnetic field, gravity, and pressure gradients.

$$\frac{\boldsymbol{\partial v_r}}{\boldsymbol{\partial\phi}}=\frac{1}{\boldsymbol{\Omega}_{\text{rot}}}\times\boldsymbol{v}_r\frac{\boldsymbol{\partial v_r}}{\boldsymbol{\partial r}} \tag{2.4}$$

solving this equation numerically using the Upwind difference scheme gives solar wind speed at L1.

$$\boldsymbol{v_{i+1,j}} = \boldsymbol{v_{i,j}} + \frac{\boldsymbol{\Delta r}\,\boldsymbol{\Omega}_{\mathrm{rot}}}{\boldsymbol{v_{i,j}}}\left(\boldsymbol{v_{i,j+1}} - \boldsymbol{v_{i,j}}\right) \tag{2.5}$$

2.1.2 Inner Heliosphere Model

PLUTO code is used in the inner heliosphere for simulation. The Pluto code solves magnetohydrodynamics (MHD) equations on a uniform grid in spherical coordinates, using finite difference or volume methods to solve conservation equations of mass, momentum, magnetic field, and energy.

MHD Setup & Numerical methods

For simulating the inner heliosphere the MHD simulation domain is specified from 0.1 AU to 2.1 AU in the radial direction, from $-60°$ to $60°$ in latitude, and from $0°$ to $360°$ in longitude with a resolution of $150 \times 120 \times 360$. The system uses a second-order Total Variation Diminishing (TVD) linear reconstruction scheme and an HLLC Riemann solver to solve the MHD equations in time on a static grid. The equations solved are:

$$\frac{\boldsymbol{\partial \rho}}{\boldsymbol{\partial t}} + \boldsymbol{\nabla} \cdot (\boldsymbol{\rho v}) = \mathbf{0} \tag{2.6}$$

$$\frac{\boldsymbol{\partial m}}{\boldsymbol{\partial t}} + \boldsymbol{\nabla} \cdot \left[\boldsymbol{mv} - \boldsymbol{BB} + \left(\boldsymbol{p} + \frac{\boldsymbol{B}^2}{2}\right)\boldsymbol{I}\right] = \boldsymbol{\rho g} \tag{2.7}$$

$$\frac{\boldsymbol{\partial B}}{\boldsymbol{\partial t}} - \boldsymbol{\nabla} \times (\boldsymbol{v} \times \boldsymbol{B}) = \mathbf{0} \tag{2.8}$$

$$\frac{\boldsymbol{\partial E_t}}{\boldsymbol{\partial t}} + \boldsymbol{\nabla} \cdot \left[\left(\frac{\boldsymbol{\rho v}^2}{2} + \frac{\boldsymbol{\gamma p}}{\boldsymbol{\gamma - 1}}\right)\boldsymbol{v} + \boldsymbol{B} \times (\boldsymbol{v} \times \boldsymbol{B})\right] = \boldsymbol{m} \cdot \boldsymbol{g} \tag{2.9}$$

where ρ represents the mass density, m is the momentum density (given by ρv), v is the velocity, B is the magnetic field, p is the isotropic thermal pressure, E_t is the total energy density, g represents gravitational acceleration, and γ (with a value of $\frac{5}{3}$) is the specific heat ratio of the solar wind plasma.

Chapter 3

Development of Automated Space Weather Pipeline

3.1 Introduction

Our objective is to create a fully automated, end-to-end space weather modeling system capable of simulating both solar wind and coronal mass ejections (CMEs) for operational use. This system is designed to integrate multiple space weather models (CME model and Solarwind model or other) into a unified, automated setup that supports seamless easy coupling. This chapter provides the methodologies and technical aspects utilized in the development of this system. Our primary objective is to create a space weather system capable of autonomously handling the full pipeline from data ingestion and processing to simulation and forecasting. The autonomous setup enables timely reliable space weather predictions.

The architecture centers around several core modules, each responsible for a specific task within the large framework. These include the automated simulating module, the automated data module, the visualization module, and the data management system that ensures smooth data flow. The pivotal modules are the simulation modules for solar wind simulation and CME simulation. MHD simulation module which uses the PLUTO code to simulate the inner heliospheric propagation. The inner heliospheric module and the coronal module of the SWASTi solar wind is our module 1 and SWASTi CME is the module 2. The Visualization module is designed to display the simulation outputs in an accessible and interactive format. By translating the data into visual representations, the module makes it easier for users to analyze the result and identify potential space weather events. The data management system is an integral part of the system. It is responsible to collecting, storing, organizing, and maintaining all the data generated by the system. Given the large amount of data, robust data management ensures both data

integrity and quick accessibility for the simulation and visualization modules.

To ensure continuous, autonomous operation, I have implemented a modular approach technique, enabling each module to function in sequence with minimal human interventions. The containerization technique is used to build the modules. we have used Docker containers. Docker containers facilitate consistency across different deployment environments and enhance scalability and simple dependency management. Container orchestration tools are employed to manage the deployment of different modules and inter-module dependencies.

This chapter will provide a detailed breakdown of the architecture, illustrating all the modules, and workflows. Through this design, we demonstrate the potential of fully automated and operational space weather simulation.

3.2 System Architecture

This is the architecture designed and developed for the automated and operational space weather system. It uses a modular and containerized setup designed to handle automated solar wind and CME simulation. The architecture diagram is shown below for a comprehensive understanding of the system's design and workflow.

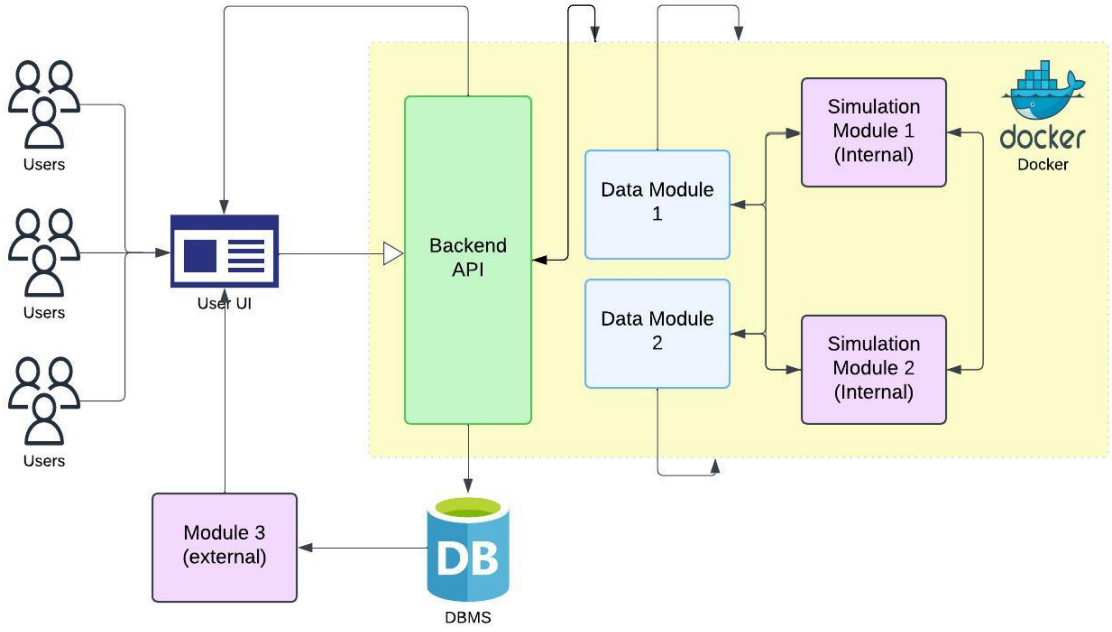

Figure 3.1: Level architecture diagram of automated space weather system

3.2.1 Simulation Modules

Simulation Module 1 and Simulation Module 2 are the internal containerized modules that run the core simulation. Each of this modules contain different programs that can simulate multiple space weather phenomena. In this work Module 1 represent the solar wind and Module 2 is for CME simulation. Both modules include the PLUTO code simulation. The detailed setup of these modules will be explained in the next sections. Both modules are connected to each other so that they can share the PLUTO code simulator. Both modules are also connected to the Data modules. The system is designed with modular data inputs to accommodate the diverse requirements of different simulations. Each simulation may require specific types of input data, sourced from various providers or datasets. This modular approach ensures flexibility and scalability, allowing the architecture to dynamically integrate and process data tailored to the unique needs of each simulation. These containers ensured that each simulation has its own isolated environment to run in parallel and avoid conflicts between other modules.

3.2.2 Data Modules

Data modules are designed specifically for the user defined input data according to the simulation requirements. Input data can be uploaded by the user to the system as well as downloaded automatically from the internet as per the information such as the date of the event. These modules operate within the Docker container. These modules are connected to the specific simulation modules and connected to the parent container. The connection to the parent container facilitates the user to upload the input data for the specified simulation.

3.2.3 Backend API

The Backend API serves several key functions in the architecture. The primary function is API enables users to interact with the system through user interface (UI). Users can initiate specific simulations, configure parameters, or view results through UI. It also allows users to monitor the progress of the simulation, track data processing, and receive notifications of the issues. These actions are carried out through the Backend API, which passes these requests for frontend and backend communications, authenticates them, and routes them to the appropriate module. API routes data from a Database management system (DBMS). It fetches raw data from the database to the module, after the simulation data will be saved to the database and receives stored simulation for users. So the backend API acts as a middle layer that allows different modules to communicate with one another.

3.2.4 Database Management System (DBMS)

The Database Management System (DBMS) is a fundamental part of the architecture, designed to organize, store, and manage all simulation data generated by the automated system. It ensures seamless integration between different modules, allowing for efficient storage and retrieval of results for further analysis.

3.2.5 Visualization Module

The visualization module (module 3 in Figure 3.1) provides a graphical representation of the simulated output. It enables users to analyze solar wind or CME predictions generated by the HUX or PLUTO models. Multiple visualization tools can be incorporated into it. This module bridges the gap between raw simulation data and actionable insights, enhancing user interpretation and decision-making.

3.3 Workflow

1. **User Interaction and Input:** Users interact with the system through a User Interface (UI), accessible via a web application. Through the UI, users can submit requests, configure parameters for data processing or simulations, and view results. Users can initiate a new simulation, request specific data analysis, or retrieve historical data for comparison.

2. **Request Handling by the Backend API:** The Backend API receives the user request from the UI. Based on the request type, the API determines the sequence of tasks that need to be executed and communicates with appropriate modules.

3. **Input data handing by Data Module:** As per user-defined events and parameters or the uploaded input data by the user, the docker orchestration container setup will initiate the input data to the respective simulation module.

4. **Simulation Initialization by Simulation Modules:** The simulation modules, containerized and isolated in Docker, use the prepared data to generate predictions or models of space weather phenomena. The containerized and isolated simulation module in the docker setup will immediately start the simulation using the input data received. The modules run independently but are orchestrated by the Backend API, ensuring they execute in the proper sequence and data flows smoothly between them. After the simulation data will be saved in DBMS.

5. **DBMS:** Simulated data will be saved to DBMS so that the user can access it. If the request requires historical or real-time data, the Backend API retrieves relevant data from the Database Management System (DBMS). This might involve fetching preprocessed data or previously run simulation results.

6. **Visualization Module:** After the simulations are completed and data saved, the results are passed to the Visualization Module for presentation to the user. The Visualization Module processes the simulation data and generates graphical representations such as charts and graphs.

3.4 Development and Automation of Solar wind simulation module

This section explains the step-by-step process for the development of the solar wind simulation module mainly including the creation of a user-facing script (main.py), the containerized simulated framework, and the database creation for the solar wind.

3.4.1 Dockerization: Solar wind Module

Dockerization of the coronal model and inner heliospheric model is the foundational step in developing this automated module. The `Dockerfile` defines the environment and workflow for the containerized solar wind simulation system. The architecture of the solar wind module is shown in Figure 3.2.

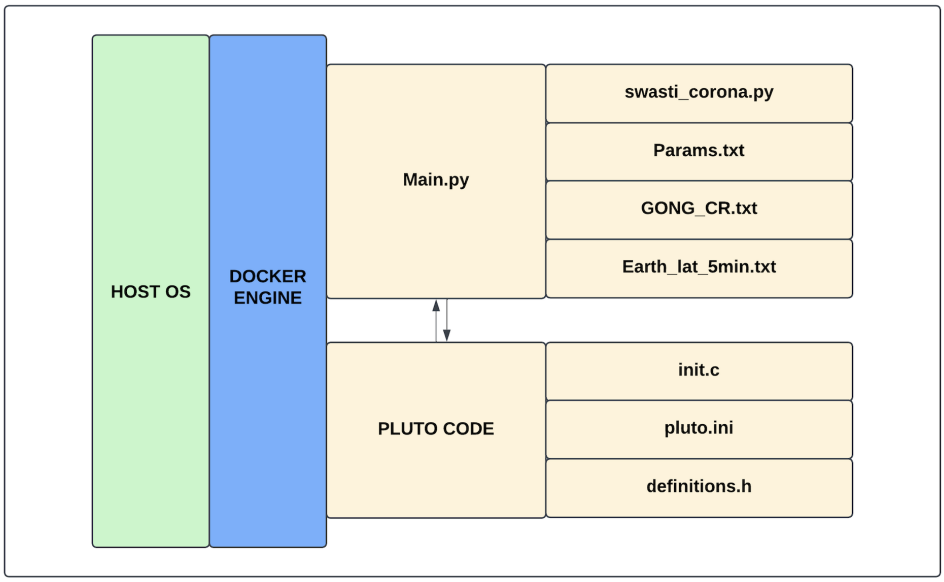

Figure 3.2: Docker container architecture of solar wind module.

Base Image and dependencies The container uses the official `python: latest` image as its base. This ensures compatibility with the Python scripts. But all the dependencies for the PLUTO code such as gcc, and openMPI are also included. The architecture of the dockerized solar wind module is designed as a modular folder approach as shown in the figure. All essential packages are included for user-friendly usage.

- `gcc` and `libhdf5-dev`: Libraries for building and linking PLUTO and other C-based programs.
- `openmpi` and `libopenmpi-dev`: Required for parallel computing using MPI.
- `valgrind` and `gdb`: Tools for debugging.

Components development The solar wind simulation module mainly consists of 2 scripts `swasti_corona.py`, `main.py`, and a simulator PLUTO code. `swasti_corona.py` is the SWASTi framework code responsible for the coronal modeling. The `main.py` scripts serve as a multi-purpose control and management module. It is specifically designed to ensure that the backend code `swasti_corona.py` remains unaffected, thereby making the automated system risk and error free. To handle this `main.py` is developed, to maintain all necessary inputs required for running the simulation and also to take care of the input parameters that the user needs to provide. So in this module `main.py` is the only file that communicates with the outside environment. we will discuss about `main.py` in detail in the upcoming sections. So by running the `main.py` using the first Run command specified inside the docker will run the coronal model and the output generated will be saved to a temporary subdirectory called `PLUTO_Input`. This sub-directory is then accessed by the PLUTO code to run the simulation.

The PLUTO code itself is highly modular and allows users to select numerical schemes and physics modules according to their simulations. It also features a detailed terminal interface. However, since our setup is fully automated, we need to choose the required configurations tailored to our simulations. So, a compatible, parallelly compiled executable is created and deployed within the Docker container. This executable is installed in the container with the required compatible setup to ensure seamless operation. The secondary run command in Docker specifically concentrates on executing the Pluto executable file automatically once the required input files are generated. Together these components form an automated solar wind simulation module along with a Docker orchestration setup.

Working Directory Setup The root directory of the container environment is `app`. It contains the `Dockerfile` and other configuration files required to build and run the

Docker image. The `pluto_run` directory is the working directory where all scripts, input files, executables, and outputs are stored. This ensures all operations and outputs are centralized in one folder for easy access and debugging. The main components of the module, such as `main.py`, `swasti_corona.py`, and the PLUTO code, are located inside the `pluto_run` directory. All generated files, logs, and results are stored here for easy accessibility.

Execution Workflow According to the user command and operation given from the user interface, the Backend API will communicate and necessary inputs will be generated in the `pluto_run` directory. The `main.py` enables the user interaction and parameter handling. We will discuss `main.py` in detail. So, the `main.py` will run `swasti_corona.py` with the Docker initial run command for the coronal model. Once the coronal model is finished running, it will make the necessary inputs for the inner heliospheric PLUTO code, and the Docker secondary run command for the PLUTO code will be initiated. It will start running the MHD simulation. Upon completion of the simulation, the output will be stored in the `pluto_run` directory.

The files `params.txt`, `GONG_CR.txt`, `Dec_adapt_HuX`, and `Earth_lat_5min.txt` are required to run the coronal model Python script `swasti_corona.py`. The `params.txt` file contains the free parameters of the WSA relation explained in Chapter 2. Similarly, `init.c`, `definitions.h` and `pluto.ini` are essential for running the PLUTO code. Along with these, the `PLUTO_Inputs` generated by the `swasti_optimization.py` script is crucial for executing the inner heliospheric MHD simulation.

Non-root User A non-root user, `nonrootuser`, is created within the container. This enhances security by preventing accidental or malicious modifications at the system level.

3.5 main.py for solar wind module

The main.py script is designed as a multi-purpose control and management script for the SWASTi framework. This Python script helps handle input parameters, execute simulations, generate results, and visualize data. Its design ensures that the backend simulation codes (`swasti_corona.py`) remain unaffected, making the system robust and maintainable. This is the only script inside the simulation module that interacts with the Backend API or the files outside the docker container. Below is a detailed breakdown of the features, capabilities, and design purpose based on the script.

Input Handling: Users can provide inputs in two primary ways: by specifying a solar event date, or by uploading custom magnetogram input files. Additionally, users can define their own free parameters for the WSA relation in the `params.txt` file. If no parameters are provided, default values will be assigned for the simulation. The SWASTi framework incorporates magnetograms from NSO-GONG and GONG-ADAPT. Additionally, daily forecasting can be enhanced by integrating ADAPT maps with daily magnetograms (Figure 3.3). This automation enables SWASTi to serve as a highly effective tool for daily space weather forecasting, offering timely and reliable updates.

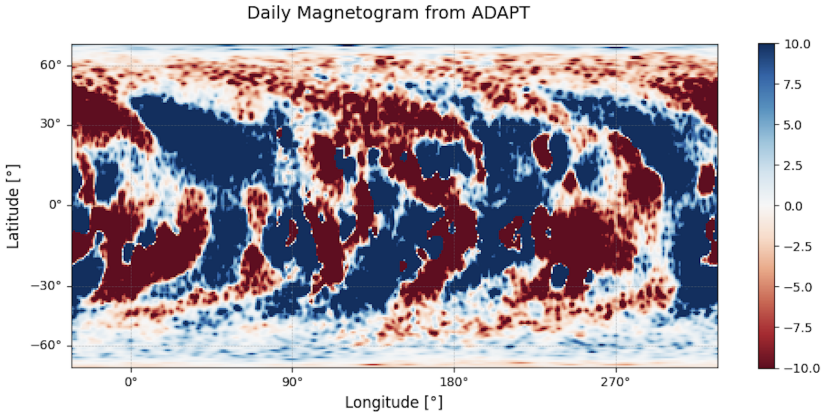

Figure 3.3: Daily magnetogram input from ADAPT on $2024-08-12, time: 06:00:00$.

Statistical study: Users have the flexibility to enable either the HUX or PLUTO code in the `main.py` script based on their simulation requirements. If users are only interested in generating the solar wind speed graph, they can opt for the HUX model and disable the PLUTO input generation. This feature streamlines the workflow for simple solar wind speed visualization without running computationally intensive simulations. For comparison with in situ data, the solar wind data received at the L1 point obtained from OMNIWeb is used. The `main.py` script generates a comparison plot between the simulated solar wind data and the OMNIWeb data, enabling users to visually assess the accuracy of the model. The `main.py` script incorporates a detailed statistical analysis to evaluate the model's performance and optimize the WSA parameters. This analysis is crucial for improving the accuracy of solar wind predictions. The statistical study includes:

1. **Correlation Coefficient (CC):**
   Measures the linear relationship between the simulated and observed solar wind speeds. A higher CC indicates a stronger correlation and better model performance.

2. **Root Mean Square Error (RMSE):**
   Quantifies the average deviation between the simulated and observed values, providing a measure of the model's predictive accuracy.

3. **Normalized Standard Deviation (STD):**
   Evaluate the variability in the simulated solar wind speeds compared to the observed data and normalized using the mean value.

4. **Sigma Calculation:**
   An error metric, σ, is calculated using the following equation:

$$\sigma = (1 - \mathrm{CC})^2 + \left(\frac{\mathrm{RMSE}}{100}\right)^2 + (\mathrm{NSD})^2 \tag{3.1}$$

   This metric combines multiple error measures to provide a comprehensive assessment of the model's accuracy.

3.6 Development of Automated pipeline for CME Forecast

As discussed in Section 3.4, the same methodology has been extended to develop a fully automated forecasting pipeline for CME (Coronal Mass Ejections). Since CMEs propagate through the background solar wind, we have integrated the previously developed automated solar wind module to provide the ambient solar wind conditions for CME propagation. Additionally, the CME setup has been fully containerized and included within the same Docker environment. As illustrated in Figure 3.1, both simulation modules—the solar wind and CME—are seamlessly integrated into the pipeline. The base Docker image, working directory structure, execution workflow, and non-root user setup remain consistent with the solar wind module.

For CME simulations, a modified version of the PLUTO code has been incorporated, allowing for the simulation of multiple CMEs. Users are required to provide key input parameters such as the event date, CME latitude, longitude, speed, and half-width angle. Other physical parameters—such as density, temperature, pressure, and magnetic flux are kept constant to simplify model usage. To enhance user accessibility and ease of use, we developed a centralized configuration file named SWASTI.INI. This file enables users to configure all simulation parameters, including the simulation date, WSA parameters for solar wind, and CME-specific inputs. Furthermore, we have included additional flexibility: users can choose to run the pipeline without the full MHD simulation and access only the HUX model output, or run a solar wind-only simulation by disabling CME propagation. This modular setup ensures a highly versatile and user-friendly experience, adaptable to various research and operational needs. Refer to the SWASTI.INI structure shown in Figure 3.4.

```
SWTI_START_TIME: 2025-04-01 12:00 # Date and time to download the input magnetogram
SWTI_INPUT_MAP: ADAPT             # Type of magnetogram to use (ADAPT or GONG)
SWTI_RUN_MHD: YES                 # Whether to run the PLUTO code for full MHD simulation
SWTI_NPROCS: 16                   # Number of processors to use for parallel execution
SWTI_INCLUDE_CME: NO              # Enable or disable CME inclusion in the simulation

# [WSA Parameters] section contains empirical WSA model parameters for solar wind speed estimation
SWTI_WSA_ALPHA: 0.222222          # Empirical alpha parameter in the WSA relation
SWTI_WSA_BETA: 1.25               # Empirical beta parameter in the WSA relation
SWTI_WSA_VMIN: 250.0              # Minimum allowed solar wind speed (km/s)
SWTI_WSA_VMAX: 650.0              # Maximum allowed solar wind speed (km/s)

# [CME Parameters] section defines the CME characteristics, required if CMEs are included
SWTI_CME_lat: 79.0                # Latitude of the CME (degrees)
SWTI_CME_lon: 33.0                # Longitude of the CME (degrees)
SWTI_CME_width: 52                # Half angular width of the CME (degrees)
SWTI_CME_speed: 1047.0            # CME speed (km/s)
SWTI_CME_onset: 1823503.0         # Onset time of CME in seconds since simulation start
```

Figure 3.4: SWASTI.INI file

The addition of CME modeling to your space weather simulation pipeline significantly increases computational time. This is mainly because CME simulation involves solving complex numerical Magnetohydrodynamic (MHD) equations with parallel processing. These simulations need high computational resources and efficient data communication to run effectively. Since our pipeline is fully automated and containerized using Docker, efficient inter-process and inter-container communication becomes crucial. The containerized architecture introduces some overhead, especially during parallel processing when modules are running inside Docker containers. This is particularly important when handling large datasets or when multiple simulation modules need to exchange intermediate results rapidly, or share information during parallel processing.

The main problem faced is running parallel simulations across multiple processes or threads (e.g., using MPI or multi-threaded solvers), fast inter-process communication is critical. In a containerized environment, using Docker's default bridge network adds layers of network abstraction that can introduce latency during data exchange between containers or between container and host processes. This overhead becomes especially problematic in automated pipelines, where multiple simulation stages must pass data back and forth efficiently and continuously. To mitigate this communication bottleneck, we enabled NAT communication by using Docker's host network mode. This enables direct access of the host machine's network stack, bypassing Docker's virtual bridge but staying inside Non root user itself. This reduces the overhead of TCP/IP routing between containers and between container and host. It allows faster access to files, data logs, simulation outputs, or shared memory. The pipeline now supports robust, scalable CME forecasting. The integration of CME modeling marks a significant milestone in the evolution of the system, enabling researchers and operational forecasters to simulate CME solar wind phenomena with minimal manual intervention, paving the way for real-time, end-to-end space weather prediction capabilities.

3.7 Database generation:

The creation of solar wind database is important for the Architecture we are developing. This dataset is created using the Heliospheric Upwind Extrapolation (HUX) model concentrating on solar minima Carrington Rotations (CR). So far we have created datasets for 2008, 2008, 2018, and 2019. The generated data will be stored in the database outlined in the architecture. This database enables easy access to past simulation results, allowing users to efficiently simulate historical events and retrieve detailed information about previously simulated events.

The dataset is created by fine-tuning the free parameter in WSA relation. Using the in situ data from OMNI web the main.py scripts optimize the V_{min}, V_{max}, β, and α. The optimization process involves iterating through the range of parameter combinations and identifying the combinations that minimize the σ value specified in equation 3.1. The optimal results for each Carrington rotation are filtered based on their σ values.

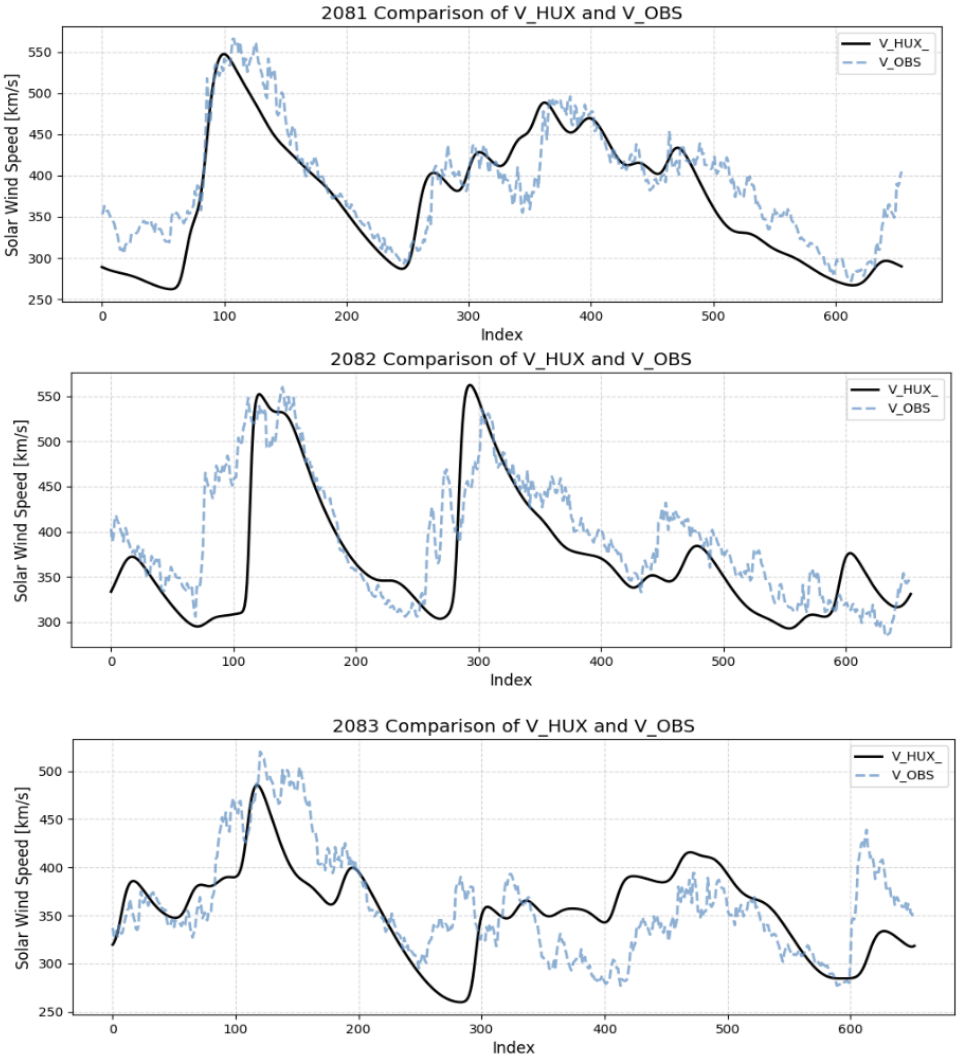

Figure 3.5: Solar wind speed plots at L1 for three consecutive Carrington Rotations (CRs) from the 2008 dataset. The blue dotted line represents the in-situ observations obtained from OMNIWeb.

These optimized results are then well structured in a CSV file, which includes the basic details about the events, statistical analysis, and corresponding optimized parameters. ASCII files are generated for each event, providing the descriptive metadata about the event and the values of solar wind speed at L1. So the dataset includes CSV files for each event, ASCII files, solar wind plots, and comparison plots with in-situ data. Some of the plots and datasets generated are given below. The comparison plot of 3.6, does not

align with the in-situ observations. As seen in the plot, features of the real data are not captured by the simulation. This plot is for the 2284th Carrington Rotation, a period marked by peak solar activity with multiple Coronal Mass Ejections (CMEs) occurring throughout the month. This discrepancy arises because the plot is generated using the solar wind module of the system, which doesn't have the specifications for CME. In future work, we plan to incorporate the CME simulation module into the system to address this issue, enabling more accurate simulations of both solar wind and CMEs.

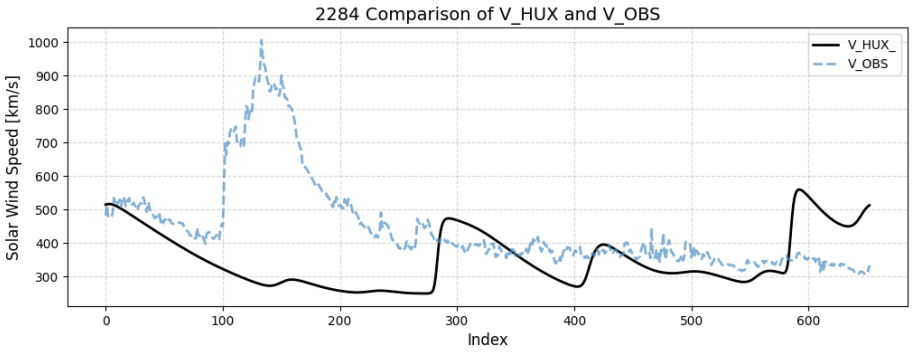

Figure 3.6: Solar wind speed plots at L1 for Carrington Rotation 2284, spanning from May 6, 2024, to June 2, 2024. Multiple powerful CMEs were reported between May 5 and May 12, 2024. As seen in the initial part of the plot, a spike in the solar wind velocity is observed in the in-situ data, corresponding to these CME events.

Year	Input CR	Start Time	End Time	V_min	V_max	Beta	Alpha	W	CC	RMSE	NSD	Sigma
2008	2067	2008-02-21 17:30:36	2008-03-20 1:15:39	240	725	1.75	0.22	0.02016317	0.44	154.3	0.13	2.711349
	2068	2008-03-20 1:15:39	2008-04-16 8:05:56	240	725	1.55	0.22	0.01491800	0.54	149.64	0.21	2.494913
	2069	2008-04-16 8:05:56	2008-05-13 13:52:40	240	725	1.7	0.22	0.01314419	0.26	125.74	0.00	2.128655
	2070	2008-05-13 13:52:40	2008-06-09 18:52:14	240	725	1.1	0.22	0.01084289	0.64	93.86	0.08	1.016970
	2071	2008-06-09 18:52:14	2008-07-06 23:36:46	240	725	1.75	0.22	0.01129859	0.75	95.95	0.05	0.985640
2009	2079	2009-01-13 22:34:11	2009-02-10 6:46:36	240	725	0.75	0.22	0.01036178	0.49	85.59	0.43	1.177565
	2080	2009-02-10 6:46:36	2009-03-09 14:45:49	240	725	0.8	0.22	0.00980443	0.45	78.84	0.22	0.972475
	2081	2009-03-09 14:45:49	2009-04-05 22:00:03	240	725	0.75	0.22	0.01044578	0.89	38.83	0.11	0.174977
	2082	2009-11-09 20:29:35	2009-12-07 3:59:36	240	725	1.7	0.22	0.00746586	-0.04	86.72	0.47	2.054536
	2083	2009-05-03 4:11:06	2009-05-30 9:25:58	240	725	0.85	0.22	0.00938294	0.54	48.23	0.19	0.480313
2019	2213	2019-01-16 19:50:06	2019-02-13 4:02:32	240	725	0.9	0.22	0.00926000	0.38	108.51	0.01	1.561942
	2215	2019-03-12 11:59:03	2019-04-08 19:08:15	240	725	0.7	0.22	0.00988665	-0.15	101.27	0.22	2.396461
	2216	2019-04-08 19:08:15	2019-05-06 1:13:52	240	725	0.7	0.22	0.00848107	-0.04	81.43	0.02	1.745084
	2217	2019-05-06 1:13:52	2019-06-02 6:24:58	240	725	0.7	0.22	0.00796930	-0.2	92.17	0.39	2.441631
	2218	2019-06-02 6:24:58	2019-06-29 11:10:22	240	725	0.7	0.22	0.01126146	0.11	59.8	0.14	1.169304
2020	2226	2020-01-06 9:06:26	2020-02-02 17:17:07	240	725	0.7	0.22	0.00729454	-0.38	109.89	0.08	3.118381
	2227	2020-02-02 17:17:07	2020-03-01 1:23:53	240	725	0.7	0.22	0.00801624	-0.41	111.13	0.14	3.242688
	2228	2020-03-01 1:23:53	2020-03-28 8:54:49	240	725	1.5	0.22	0.00781035	0.27	66.99	0.08	0.988066
	2229	2020-03-28 8:54:49	2020-04-24 15:25:38	240	725	1.2	0.22	0.00706064	-0.21	90.32	0.16	2.305470
	2230	2020-04-25 4:14:39	2020-05-21 5:20:18	240	725	1.7	0.22	0.01702421	0.41	125.98	0.14	2.594796

Table 3.1: Solar wind dataset for the years 2008, 2009, 2018, and 2019, corresponding to solar minima. The dataset includes results from HUX simulations, with CC, RMSE, and NSD values derived from comparisons with in-situ data

Chapter 4

Event simulation

4.1 Introduction

The active phase of Solar Cycle 25, which began in late 2019, has been marked by various high-frequency and intensity of solar eruptive phenomena like Coronal Mass Ejections (CMEs). Throughout 2024, multiple geoeffective CMEs were observed, many of which led to significant space weather impacts near Earth. This period of heightened solar activity offers a valuable opportunity to assess and validate space weather modeling frameworks under dynamic heliophysical conditions. In the second part of this thesis, we leverage this active solar phase to conduct a detailed analysis of selected CME events, with the goal of evaluating the performance of the automated simulation pipeline (SWASTi) developed in the earlier phase of this work.

For the first time, we incorporate in-situ observational data from Aditya-L1 SWIS, India's maiden solar observatory positioned at the L1 Lagrangian point, to directly compare model outputs with real-time solar wind measurements. This comparison focuses on event-wise simulations of CME propagation using the Automated pipeline for CME CONE simulation, SWASTi FRi3D model for CME Flux rope model simulation and contrasts them against in-situ data from the SWIS and MAG instruments aboard Aditya-L1. Specifically, we analyze CME events occurring during Carrington Rotations 2288, 2289, and 2290 each of which featured multiple CMEs with clear propagation signatures.

4.2 Model details

To simulate the selected CME events, we employ two distinct modeling approaches. The first approach utilizes the elliptical cone model, a simplified kinematic representation where the CME is treated as a non-magnetic, ellipsoidal plasma cloud. This structure

is injected into the simulation domain with uniform initial parameters, including radial velocity (V_{cme}), density (ρ_{cme}), and temperature (T_{cme}). The model assumes a homogeneous distribution of plasma properties and is particularly useful for rapidly simulating CME trajectories and arrival times under minimal magnetic complexity. The automated SWASTi pipeline is employed to simulate events using this cone model. The architecture and workflow of this pipeline are described in detail in Chapter 3.

The second approach involves the Flux rope model (Isavnin [2016]), which offers a more physically realistic depiction of CME morphology and internal structure. This model generates a magnetized 3D flux rope with a croissant-like geometry, connected at the solar surface and extended to 0.1 AU. The FRi3D-based CME preserves a consistent internal plasma density and temperature, while its velocity structure is derived from the local toroidal speed along the flux rope. This method allows for a more accurate simulation of the CME's magnetic configuration, making it suitable for analyzing events with pronounced magnetic signatures. The simulation setup and implementation details for both the cone model (via the pipeline) and the FRi3D model will be explained in the upcoming section of this chapter.

4.3 Aditya L1 - SWIS

The Solar Wind Ion Spectrometer (SWIS) is a key component of the Aditya Solar Wind Particle Experiment (ASPEX) aboard the Aditya-L1 mission. It is specifically designed for in-situ measurements of solar wind ions, enabling detailed studies of solar wind composition and dynamics. SWIS consists of two independent hemispherical electrostatic analyzers with a "top hat" geometry THA-1 and THA-2 providing nearly full angular coverage. THA-1 is equipped with a magnetic mass analyzer for species differentiation, while THA-2 is purely electrostatic. The system incorporates two fundamental measurement techniques: integrated flux measurement using a Faraday Cup (FC) and energy-resolved flux measurement using an Electrostatic Analyzer (ESA). While FCs offer a straightforward and reliable method for determining bulk solar wind parameters (Kasper [2002]), ESAs are more appropriate for detailed investigations into the directional anisotropies within the solar wind.

These instruments operate by selecting ions based on their energy-per-charge through electrostatic deflection, then, in the case of THA-1, further separating them by mass-to-charge using a magnetic sector. By systematically scanning over a range of energies and angles, the instrument builds up a comprehensive map of the velocity distribution of incoming solar wind ions. THA-1 is additionally equipped with a magnetic mass

analyzer placed after the electrostatic analyzer. This magnetic sector analyzer introduces a magnetic field perpendicular to the ion trajectory, allowing ions to be separated further based on their mass-to-charge ratio (M/q). This enables identification of major solar wind constituents, such as protons (H^+), alpha particles (He^{2+}), and heavier ions. On the other hand, THA 2 is a purely electrostatic analyzer and serves to provide a complementary measurement of energy spectra and angular distributions. Together, these analyzers cover nearly 360° in azimuth and 90 degrees in elevation, enabling a complete 3D sampling of the velocity distribution of ions as they arrive at the spacecraft. SWIS is capable of measuring ions in the energy range of 100 eV/q to 20 keV/q, encompassing the full spectrum of the solar wind and its various components.

SWIS instruments, which include electrostatic analyzers (ESAs) and Faraday Cups (FCs), are designed to detect individual solar wind particles and measure both their energies and arrival directions. To cover a wide range of particle energies, the instrument varies the voltage applied to its electrostatic plates, allowing only particles with a specific energy-to-charge ratio (E/q) to pass through at any given time. By systematically scanning across a broad spectrum of energy and angular bins, these instruments record the number of particles arriving from each direction and within each energy interval. This process yields the differential flux, providing detailed insight into the solar wind's energy and directional distribution. Once the velocity distribution function is reconstructed by applying standard statistical analysis in velocity space, and assuming the entire velocity distribution function lies within the energy range sampled by the Faraday Cup for the given spectrum, the proton number density, average speed and temperature are derived from the moments of velocity distribution function which is maxwellian for the FC. SWIS also identifies and characterizes different ion species present in the solar wind, such as protons, alpha particles, and heavier ions. By measuring parameters such as energy-per-charge and time-of-flight, the instruments can distinguish ions with different masses and charges. This capability allows SWIS to infer the relative abundance of various ion populations and to study compositional variations across solar wind streams and transient events. These bulk properties serve as essential inputs for modeling solar wind dynamics and understanding its interactions with planetary magnetospheres and interplanetary structures. In our event simulation, we also use SWIS data as a reference for comparative analysis.

4.4 Event Description

The months spanning late August to last November 2024 witnessed multiple CMEs, each with distinct characteristics. This sequence occurred during Carrington Rotations (CR) 2288, 2289, and 2290. Carrington Rotations refer to a system of measuring solar rotations, where each rotation corresponds to approximately 27.3 days, based on the tracking of sunspots or the reappearance of eruptions. These events are particularly chosen not only for their space weather relevance, but also because they coincided with the operational phase of Aditya-L1. For the first time, data from Aditya-L1 were incorporated into CME validation efforts, offering a new observational perspective to assess and refine our simulation outputs. Each of the selected CRs contains multiple CME events, including full-halo and partial-halo structures, with varying degrees of geoeffectiveness observed at L1.

4.4.1 Event Description: Carrington Rotation (CR) 2288

Carrington Rotation (CR) 2288 spanned from August 23, 2024, 08:04 UT to September 19, 2024, 14:17 UT, and was characterized by moderate solar activity. During this period, multiple Coronal Mass Ejections (CMEs) were observed, primarily originating from active regions AR 13794, AR 13807, AR 13814, and AR 13815, as reported by NOAA's Space Weather Prediction Center (SWPC). Although several of these CMEs were Earth-directed and produced interplanetary shocks, they largely resulted in glancing blows—interacting with Earth's magnetosphere at oblique angles and thereby producing limited geomagnetic effects. Their associated Kp index values remained below 5, suggesting weak geomagnetic disturbances. As such, these events were excluded from the modeling efforts in this study to focus on solar eruptions with higher geoeffectiveness and stronger terrestrial impact.

A notable and significant space weather event during CR 2288 occurred on September 14, 2024, when Active Region (AR) 13825, situated at solar coordinates S18E55, produced a powerful X4.5-class solar flare—one of the most intense flares recorded during this rotation. The flare was associated with the eruption of a fast, wide CME that expelled a substantial volume of coronal plasma into the heliosphere. This powerful flare was associated with the launch of a bright, fast CME that ejected a significant volume of plasma into the heliosphere. This CME is started at 2024-09-14 15:36 UT (SOHO: LASCO/C2) and arrived at 21.5 $R_{\odot}$ at 2024-09-14 18:08 UT.

This eruption was accompanied by a large-scale coronal wave that propagated across a vast portion of the lower corona. Observations from multiple extreme ultraviolet (EUV)

channels revealed the dynamic nature of the event: intense flare brightening was evident in SDO 131 Å, fast-moving ejecta were best captured in GOES 284 Å, and a large, fast-propagating EUV wave, extending toward the northwest, was visible in the SDO 171 Å and 193 Å channels. This EUV wave traversed nearly half of the solar disk, underscoring the energy and scale of the eruption. The event subsequently drove significant geomagnetic activity at Earth, with the planetary Kp index peaking at 7.67. It culminated in a major geomagnetic storm, marked by a Dst index minimum of -120 nT recorded around 09:00 UT on September 17, 2024. Given its magnitude and comprehensive observational coverage, this CME was selected for detailed simulation and modeling in this study using both the Flux Rope and CONE-based models.

4.4.2 Event Description: Carrington Rotation (CR) 2289

Carrington Rotation (CR) 2289 spanned from September 19, 2024, 14:17 UT to October 16, 2024, 21:04 UT and was characterized by elevated solar activity. During this interval, multiple Coronal Mass Ejections (CMEs) were observed, predominantly originating from active regions AR 13835, AR 13842, AR 13844, and AR 13852, as reported by NOAA's Space Weather Prediction Center (SWPC). Although several of these eruptions were Earth-directed and did produce interplanetary shocks, their geomagnetic consequences were limited. Most of these CMEs were associated with Kp index values below 5, indicating weak disturbances and glancing interactions with Earth's magnetosphere. Consequently, these events were excluded from the modeling scope in this study.

However, two major solar eruptions during CR 2289 were identified as highly geoeffective and have been selected for detailed simulation . These eruptions originated from Active Regions AR 13842 and AR 13848 and were associated with strong X-class flares and full halo CMEs.

The first CME occurred on October 3, 2024, when AR 13842 produced a powerful X9.0-class flare, one of the most intense events during this rotation. The CME was detected in SOHO/LASCO at 12:48 UT and reached a heliocentric distance of 21.5 $R_{\odot}$ by 2024-10-03 16:29 UT. The X9.0 flare from AR 13842 was prominently observed across multiple wavelengths, with the most significant activity captured in SDO AIA 131 Å , beginning at 2024-10-03T12:08Z and peaking at 12:18Z. The eruption was also observed as an EUV wave and coronal dimming seen in SDO AIA 171/193 Å and GOES SUVI 284 Å, along with noticeable surface brightening observed in SDO AIA 304 Å imagery. Upon the arrival, this CME generated a shock signature marked by a sharp increase in interplanetary magnetic field components (Bz jumped from 6.16 nT to 14.46 nT, and Bt increased from 8.41 nT to 14.94 nT, later peaking at 16.2 nT). Bz remained mostly

positive during the initial phase. The event resulted in a major geomagnetic storm, with the planetary Kp index reaching 8.

The second significant eruption took place on October 9, 2024, when AR 13848, located at N13W08, produced an X1.8-class flare associated with a bright, fast full halo CME. Coronagraphic imagery by SOHO and STEREO-A shows a full halo CME first seen at 02:30 UTC in LASCO/C3. This CME originated at 02:12 UT and reached 21.5 $R_{\odot}$ by 2024-10-09 04:16 UT. This eruption was particularly noteworthy for the large-scale EUV wave, widespread coronal dimming, and formation of bright post-eruptive arcades. It was also preceded by the slow eruption of a very large filament located to the northeast of AR 13848, which began as early as 22:19 UT on October 8, 2024, spanning from N20W15 to N15W55 (DONKI catalogue). This CME led to a severe geomagnetic storm upon arrival at Earth, with a maximum Kp index of 8.67 and a Dst index minimum of -335 nT.

4.4.3 Event Description: Carrington Rotation (CR) 2290

Carrington Rotation 2290 spanned from October 16, 2024, 21:04 UT to November 13, 2024, 04:16 UT. During this interval, several Coronal Mass Ejections (CMEs) were detected, primarily emanating from active regions NOAA 13869, 13877, and 13883. Although many of these eruptions were directed towards Earth and were accompanied by interplanetary shocks, their geoeffectiveness was minimal. Most of the associated Kp index values remained below 5, indicating relatively weak geomagnetic impacts, likely due to their glancing trajectories and limited magnetic coupling with Earth's magnetosphere. As a result, these events were not included in this study's simulation focus. However, two significant CMEs during this rotation exhibited sufficient intensity and well-observed eruption characteristics, making them suitable for detailed modeling.

This CME originated from Active Region (AR) 13873 on 2024-10-26 06:48 , located at solar coordinates S16E60. The eruption was associated with two flares that occurred in close succession: an M9.5 flare at 06:23 UT and an X1.8 flare at 07:19 UT. The CME appeared as a partial halo directed toward the southeast in SOHO LASCO C2/C3 and STEREO-A COR2 imagery. Multi-wavelength observations from SDO AIA 131, 171, 193, and 304 Å revealed a broad field line opening near the southeast limb beginning around 06:30 UT, followed by the formation of bright post-eruptive arcades around 07:50 UT. The geomagnetic response peaked at a Kp index of 6 on October 28, indicating moderate storm conditions (G1-G2 class). The second CME was associated with a large-scale filament eruption extending from approximately S37W25 to S15W90, likely reaching beyond the western limb. The CME started on 2024-10-29 13:23. The eruption began

around 12:40 UT, as observed in SDO AIA 131, 171, 193, and 304 Å channels. The CME manifested as a partial halo directed southwestward in SOHO LASCO C3 imagery and reached 21.5 $R_{\odot}$ by 2024-10-29 18:13 UT, indicating a fast and expansive eruption with potential heliospheric impact.

4.5 Simulation Setup

The above-listed events have been simulated using two different modeling approaches within the SWASTi framework: the SWASTi-CONE model and the Flux Rope model. For the CONE model, we employed the developed automated pipeline (refer Chapter 3) to simulate the CME events, enabling consistent and efficient processing of multiple events. In the case of the Flux Rope model, the simulations were carried out using the standalone code setup of SWASTi-FRI3D, allowing detailed modeling of the CME's internal magnetic structure. The SWASTi framework encompasses both the coronal model and the inner heliospheric model, where MHD simulation is used (as detailed in chapter2). For this study, we have optimized and identified the best-fit parameters for both models by comparing simulation outputs with in-situ OMNI and ACE data for all the events selected. This section provides a detailed explanation of the simulation methodologies used for both the CONE and Flux Rope models across Carrington Rotations 2288, 2289, and 2290. It also presents the heliospheric input parameters, the setup of the CONE model pipeline, and the CME event-specific parameters used in the simulations.

4.5.1 Simulation Using the Automated Pipeline

The automated pipeline developed as part of the initial phase of this project has been utilized for simulating CME events using the CONE model. The pipeline is designed for ease of use, enabling the setup of simulations through a single configuration file, `SWASTI.INI`, where solar wind parameters and CME event-specific inputs can be specified. This configuration file includes both the heliospheric model parameters for the CONE simulation and the parameters for the inner heliospheric MHD model. Detailed documentation of the pipeline is provided in Chapter 3.

For the solar wind background, we employed ADAPT synoptic magnetograms as observational inputs for all CR selected. These magnetograms serve as input for the Automated pipeline. As described in Chapter 2, the initial solar wind speed (V_r) at 0.1 AU is derived using a modified version of the Wang-Sheeley-Arge (WSA) empirical relation (Equation 2.1). The WSA relation includes several free parameters: $V_{\min}$, $V_{\max}$, β, and

α. Additionally, the flux expansion factor (f_s) and the footpoint distance from the coronal hole boundary (d) are computed based on the magnetic field extrapolated from the input magnetogram. To enhance the accuracy of the background solar wind model, we performed an optimization of the WSA free parameters using in-situ solar wind observations from OMNI data. The WSA-predicted velocity at 0.1 AU is propagated to 1 AU using the HUX (Heliospheric Upwind Extrapolation) model, a 1D numerical scheme that neglects magnetic field, pressure, and gravity, while offering a reliable approximation of solar wind speed at L1. To identify the best-fit parameter set, we conducted a statistical comparison between the HUX-extrapolated solar wind speed at 1 AU and the OMNI in-situ measurements at L1, using the correlation coefficient (CC) and root mean square error (RMSE) as evaluation metrics . The final set of optimized WSA parameters for each Carrington Rotation is summarized in Table 4.1.

CR	$V_{\min}$ (km/s)	$V_{\max}$ (km/s)	β	α
2288	250	650	1.25	0.222222
2289	250	650	1	0.222222
2290	250	650	1.5	0.222222

Table 4.1: Optimized WSA Parameters for Each Carrington Rotation

The remaining initial conditions for the MHD inputs are derived using the given empirical relations that characterize the properties of the fast solar wind.

$$n = n_0 \left(\frac{V_{fsw}}{V_r} \right)^2 \tag{4.1}$$

$$B_r = \mathrm{sgn}(B_{\mathrm{corona}})\, B_0 \left(\frac{V_r}{V_{fsw}} \right) \tag{4.2}$$

$$B_\phi = -B_r \sin\theta \left(\frac{V_{\mathrm{rot}}}{V_r} \right) \tag{4.3}$$

In these equations, n represents the plasma number density, while B_r and B_ϕ denote the radial and azimuthal components of the magnetic field, respectively. The term $\mathrm{sgn}(B_{\mathrm{corona}})$ indicates the polarity of the extrapolated coronal magnetic field. V_{rot} refers to the rotational velocity at the inner boundary, determined by the temporal span of the magnetogram used. The constants n_0 and B_0 represent the number density and magnetic field strength associated with the fast solar wind at speed V_{fsw}. In this study, the initial conditions were defined using standard values for each Carrington Rotation (CR). The n_0, B_0, V_{fsw} were assigned specific values as follows:

- **CR 2288:** $n_0 = 200\,\mathrm{cm}^{-3}$, $B_0 = 300\,\mathrm{nT}$, $V_{\mathrm{fsw}} = 5750\,\mathrm{km/s}$

- **CR 2289:** $n_0 = 200\,\mathrm{cm}^{-3}$, $B_0 = 200\,\mathrm{nT}$, $V_{\mathrm{fsw}} = 600\,\mathrm{km/s}$
- **CR 2290:** $n_0 = 200\,\mathrm{cm}^{-3}$, $B_0 = 200\,\mathrm{nT}$, $V_{\mathrm{fsw}} = 600\,\mathrm{km/s}$

For all simulations, the initial thermal pressure at 0.1 AU was set to a constant value of 6.0 nPa. The meridional and azimuthal velocity components, V_θ and V_ϕ, were initialized to zero.

The cone model assumes a simplified, nonmagnetic geometric structure. In contrast, the flux rope model captures the complex three-dimensional magnetic field configuration inherent to CME structures, allowing for a more physically realistic representation (P. Mayank et al., 2023). For simulations using the flux rope model, we employed a standalone implementation of the SWASTi-FRI3D code. In this setup, the magnetic field inputs associated with the CME were imposed at the inner boundary of the MHD domain. So the CME input parameters we used for both the models are given in the table 4.2, 4.3, 4.4. The CME's half-width and half-height were both set equal to its half-angle to simplify the geometry. Key CME properties such as arrival time, speed at 21.5 R_s, and the eruption location on the solar surface were listed in the table.

Table 4.2: Initial Properties of CMEs Associated with CR2288

Parameters with Different Values for Each CME							
CME	**Tonset** (UT)	**Time at 21.5 $R_\odot$** (UT)	v_{CME} (km/s)	θ_{CME} (deg)	ϕ_{CME} (deg)	φ_{hw} (deg)	φ_{hh} (deg)
CME1	2024-09-14 15:36	2024-09-14 18:08	1070	8	-50	51	51
Parameters with Common Values for All CMEs							

$T_{\mathrm{CME}} = 0.8$ MK $\quad \rho_{\mathrm{CME1}} = 20 \times 10^{-19}$ kg m^{-3} $\quad P_{\mathrm{CME1}} = \rho_{\mathrm{CME1}} \times T_{CME1}$

Table 4.3: Initial Properties of CMEs Associated with CR2289

Parameters with Different Values for Each CME							
CME	**Tonset** (UT)	**Time at 21.5 $R_\odot$** (UT)	v_{CME} (km/s)	θ_{CME} (deg)	ϕ_{CME} (deg)	φ_{hw} (deg)	φ_{hh} (deg)
CME1	2024-10-03 12:48	2024-10-03 16:29	863	-4	-3	53	53
CME2	2024-10-09 02:12	2024-10-09 04:16	1509	13	8	45	45
Parameters with Common Values for All CMEs							
$T_{CME} = 0.8$ MK	$\rho_{CME1} = 20 \times 10^{-19}$ kg m^{-3}	$\rho_{CME2} = 20 \times 10^{-19}$ kg m^{-3}					

Table 4.4: Initial Properties of CMEs Associated with CR2290

Parameters with Different Values for Each CME							
CME	**Tonset** (UT)	**Time at 21.5 $R_\odot$** (UT)	v_{CME} (km/s)	θ_{CME} (deg)	ϕ_{CME} (deg)	φ_{hw} (deg)	φ_{hh} (deg)
CME1	2024-10-26 06:48	2024-10-26 08:52	1677	-19	-34	54	54
CME2	2024-10-29 13:23	2024-10-29 18:13	1047	-21	33	52	52
Parameters with Common Values for All CMEs							
$T_{CME} = 0.8$ MK	$\rho_{CME1} = 20 \times 10^{-19}$ kg m^{-3}	$\rho_{CME2} = 20 \times 10^{-19}$ kg m^{-3}					

Chapter 5

Results

5.1 Result: CR 2288

The first event simulation, spanning from August 23, 2024, 08:04 UT to September 19, 2024, 14:17 UT, includes a single CME. This CME reached a radial distance of 21.5 $R_\odot$ and entered the simulation domain on September 14, 2024, at 18:08 UT. In Figure 5.1 and Figure 5.2 snapshots of the CME simulation results are presented. plot (a1) shows the velocity distribution, while plot (b1) shows the scaled density profile of the cone CME, and (a2) and (b2) show the flux rope model result. The CME is initiated at a latitude of 8° and a longitude of −50°. The mass density of the CME is set to 2×10^{-18} kg/m^3, and the temperature is initialized at 0.8 MK. For simplicity, the half-width and half-height of the CME are assumed to be equal, both having an angular extent of 51°. Although both the cone and flux rope CMEs were initiated simultaneously and propagated through the same ambient medium, they exhibited notably different evolutionary behaviors. The cone model CME propagated at a higher speed compared to the flux rope CME and appeared to span a broader region in the r–ϕ plane, as evident in Figure 5.1 (a1).

The interaction between a CME and Stream Interaction Regions (SIRs) is crucial in altering the CME's shape and dynamics. These interactions can disrupt the self-similar expansion of the CME and have a substantial impact on its overall trajectory Winslow et al. [2021]. In this case, as the CME propagated, it encountered two SIRs along its path. When the CME exited the simulation domain, its eastern and western flanks were embedded within different SIRs, as shown in Figure 5.3.

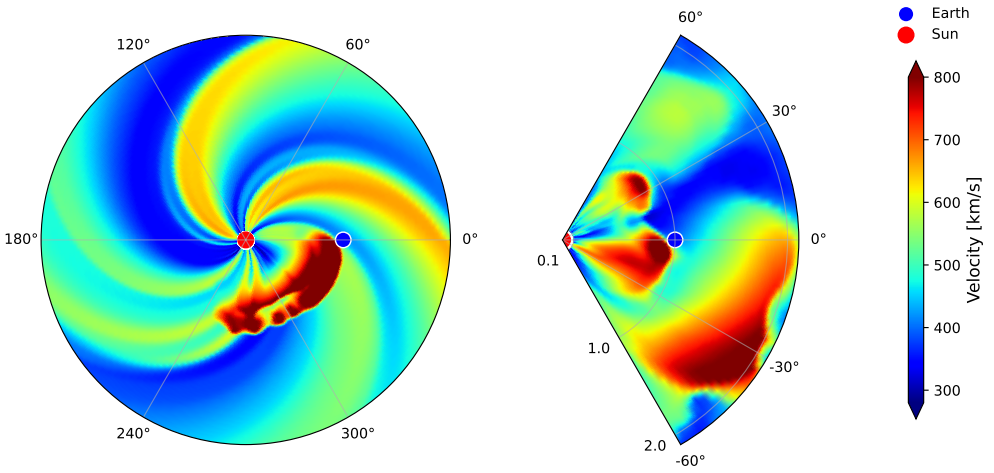

(a1) CONE speed (km/s)

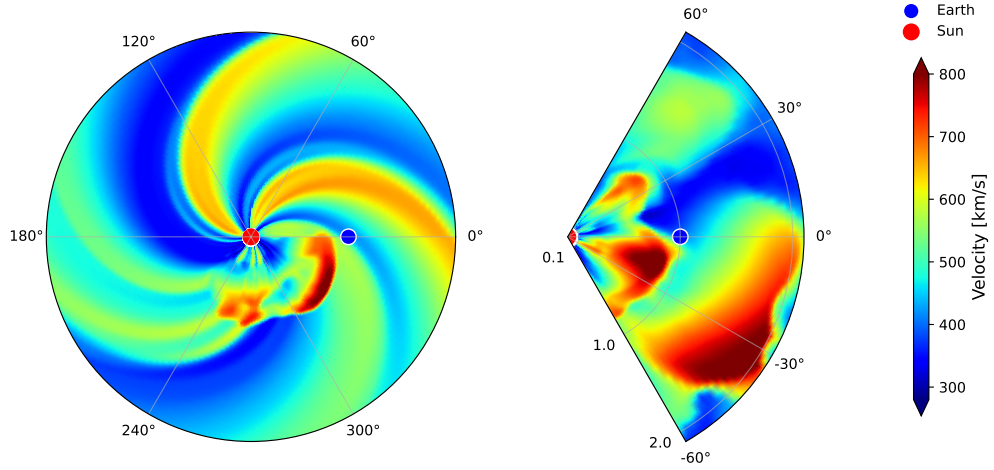

(a2) FR speed (km/s)

Figure 5.1: Time snapshot of MHD simulation solar wind speed for CR 2288 using (a1) the Cone CME model and (a2) the Flux Rope (FR) CME model.

This interaction with the SIRs led to a distortion of the CME front, particularly in its arc-like structure, which is clearly visible in the density plots in Figure 5.2. The influence of the two SIRs caused the CME to appear nearly bifurcated, as depicted in the FRI3D model visualization in Figure 5.1 a2. However, the SIRs were not sufficiently strong to significantly confine or trap the CME for an extended period. As a result, the CME continued its propagation in the original direction, albeit with some enlargement and deviation in the direction of the SIR.

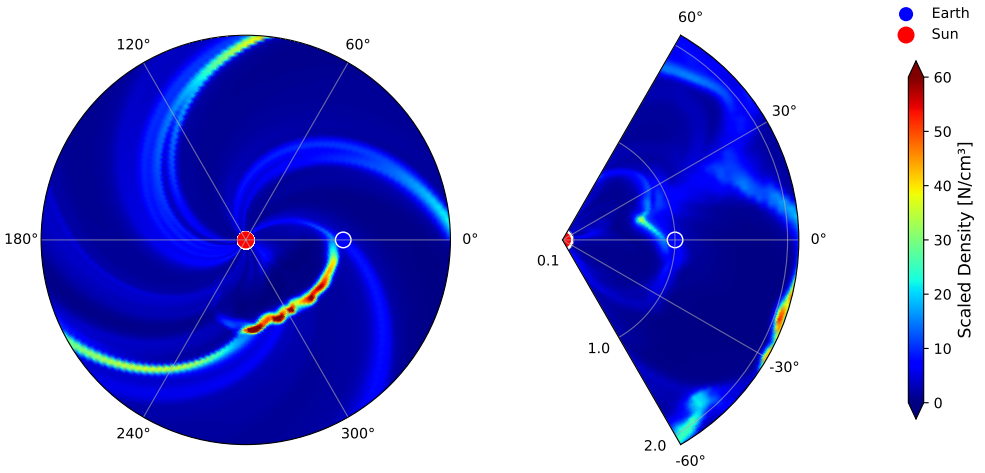

(b1) CONE scaled density (N/cm)

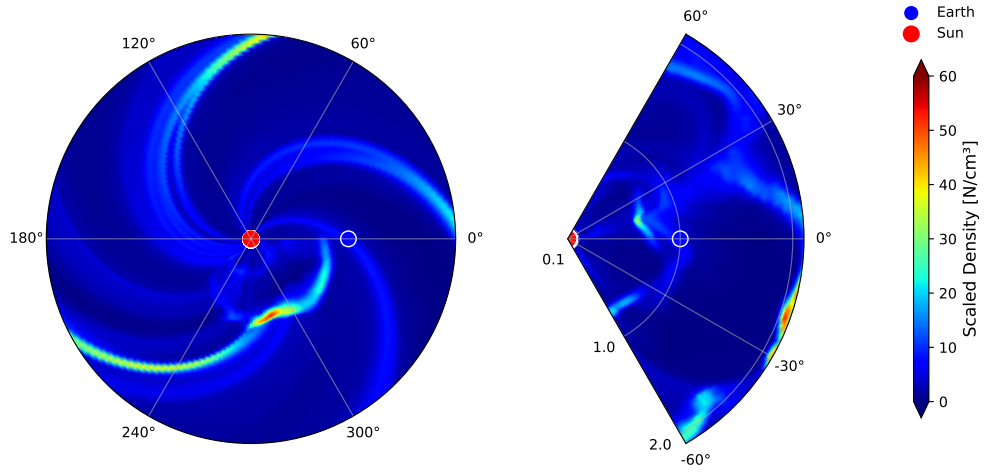

(b2) FR scaled density (N/cm)

Figure 5.2: Time snapshot of MHD simulation scaled density for CR 2288 using (b1) the Cone CME model and (b2) the Flux Rope (FR) CME model.

The velocity gradients induced by the contrasting fast and slow solar wind streams also introduced disparities in the pressure gradients and drag forces acting on different parts of the CME especially between its central region and leading edge. The slower wind streams, being denser and more pressurized, had a pronounced effect on the CME's expansion. Consequently, the CME's eastern flank experienced significant overexpansion, while the western flank, in direct interaction with a SIR, showed restricted expansion along with a noticeable deflection toward the SIR. This asymmetric expansion behavior altered the internal density distribution of the CME. Overall, variations in the speed and structure of the surrounding solar wind introduced substantial changes to the CME's density profile and dynamic evolution.

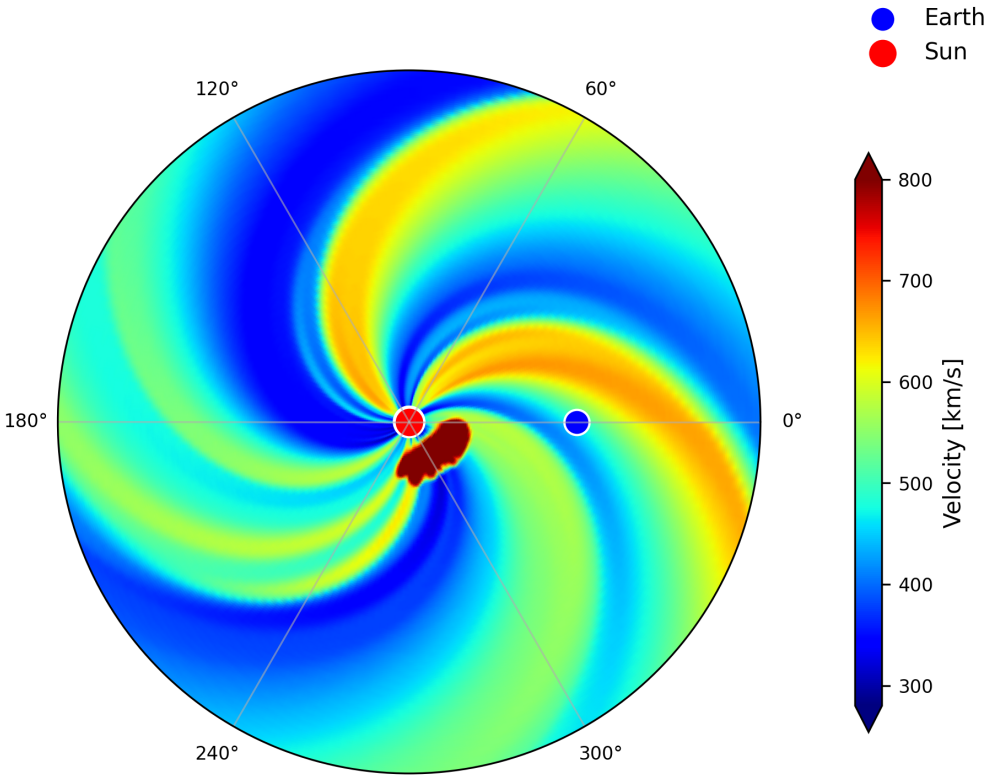

Figure 5.3: CME Propagation Starting at Latitude 8° and Longitude -50° and Interaction of Eastern and Western Ends of the CME with Two Stream Interaction Regions (SIRs)

5.1.1 Validation with in situ Measurements

To assess the accuracy of the CME modeling, a comparative analysis was carried out between the simulation results and the in situ observations from the Aditya-L1. Figure 5.4 displays time-series plots for Carrington Rotation (CR) 2288, shows the outputs from both the cone and flux rope (FR) CME models, alongside the Aditya-L1 and OMNI data at 1 AU. The cone CME model is represented by a red solid line, while the flux rope model is shown in blue. The Aditya-L1 in-situ measurements are depicted in green, and the OMNI dataset is marked in black. The shaded region highlights the temporal interval during which the CME is present. This interval is clearly distinguishable from the ambient solar wind background.

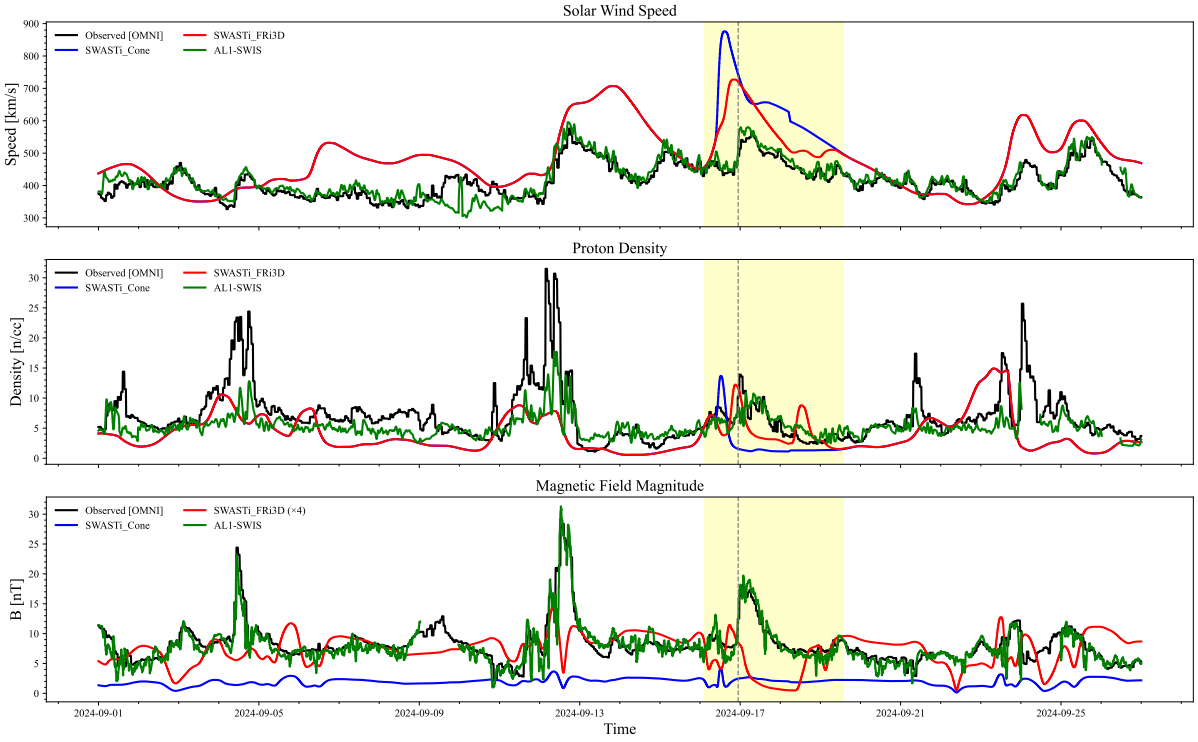

Figure 5.4: Time-series Plot of In Situ Measurements at 1 AU for CR 2288: Simulated Results for FR and Cone CMEs (Blue and Red), Aditya L1 Observed Data (Green), and OMNI Observed Data (Black). Vertical Dashed Lines Mark CME Arrival Time at Earth, with the Shaded Region Indicating CME Simulated. All Data is 1-Hour Moving Average.

In the case of CR 2288, the flux rope (FR) CME model demonstrated a more accurate prediction of the CME arrival time compared to the cone model. While both models predicted the CME's arrival at Earth's location, the cone CME exhibited a larger deviation from the actual arrival time. This discrepancy is clearly illustrated in the velocity and density subplots in Figure 5.4. For CR 2238, both the FR and cone CME models provided reasonably accurate estimates of the arrival time. In this case, the cone CME arrived earlier than observed, whereas the FR CME arrived slightly later. The FR CME model predicted the CME arrival with a delay of -2.65 hours, closely matching the observed event. In contrast, the cone model predicted an earlier arrival, with a significantly larger delay of -8.23 hours. These results suggest that while both models have predictive value, the FR model offers improved temporal accuracy in CME arrival predictions.

Similar to the arrival time predictions, the Flux Rope (FR) model provided a more accurate estimation of CME speed compared to the Cone model. The FR CME achieved a correlation coefficient (CC) of 0.75 and a root mean square error (RMSE) of 77.90 km/s when compared with the Aditya-L1 in-situ observations. In contrast, the Cone CME showed a lower CC of 0.60 and a higher RMSE of 125.57 km/s. In terms of density predictions, the FR model again outperformed the Cone model, yielding a higher CC of

0.31 and a lower RMSE of 2.95 N/cm, compared to the Cone model's CC of only 0.06 and a larger RMSE of 3.85 N/cm. The complete set of statistical values is provided in Table 5.1.

A noticeable difference is observed in the in situ magnetic field profiles between the cone and FR CME models. The FR CME shows a closer agreement with the magnetic field features detected at L1, indicating a similar pattern with the observational data. However, despite this pattern, the estimated magnetic field magnitude from the FR model does not fully align with the in situ measurements, highlighting a limitation in accurately capturing the field strength.

Table 5.1: Statistical Comparison of CME Models for CR 2288 Based on 1-Hour Moving Average Values of Speed and Density Against Aditya-L1 Observations

	Speed Metrics				**Density Metrics**			
Model	**CC**	**RMSE**	**STD**	**Σ**	**CC**	**RMSE**	**STD**	**Σ**
Cone Model	0.601	125.57	0.443	1.932	0.057	3.85	0.393	1.044
FR Model	0.745	77.90	0.371	0.809	0.314	2.95	0.380	0.616

5.2 Result: CR 2289

In this event, we simulated two CMEs. CME1 was started on 2024-10-03 at 12:48 UT and entered the simulation domain at 16:29 UT. As illustrated in velocity and density plot Figure 5.5 and Figure 5.6, the CME1 eruption was initiated from a latitude of $-4°$ and a longitude of $-3°$. To simplify the modeling process, the CME was assigned a symmetric angular extent with a half-width and half-height of 53°. Snapshots of the evolution of CME2 are shown in Figure 5.7. CME2 was initiated on 2024-10-09 at 02:12 UT and entered the simulation domain at 04:16 UT. This CME propagated at a latitude of 13° and a longitude of 8° and half-width and half-height of 45°. For consistency across both simulations, the initial mass density for each CME was set to 2×10^{-18} kg/m^3, and the initial plasma temperature was defined as 0.8 MK.

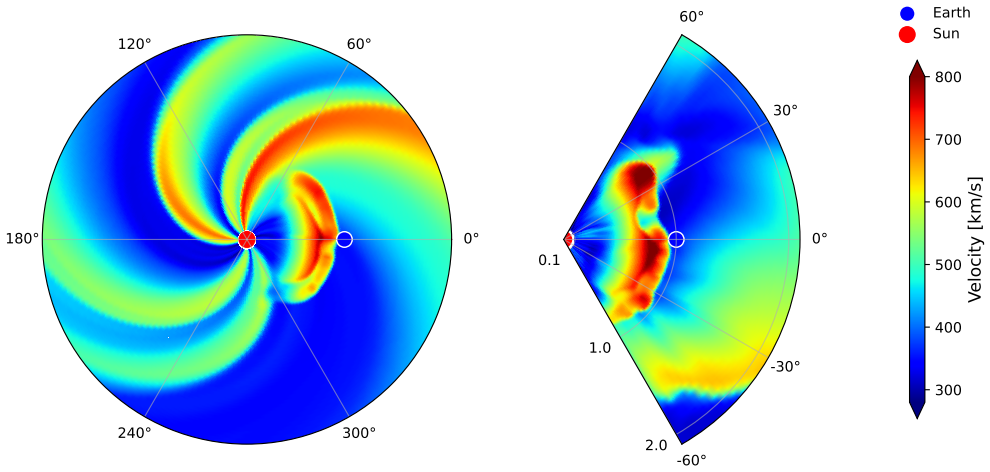

(a1) CONE speed (km/s)

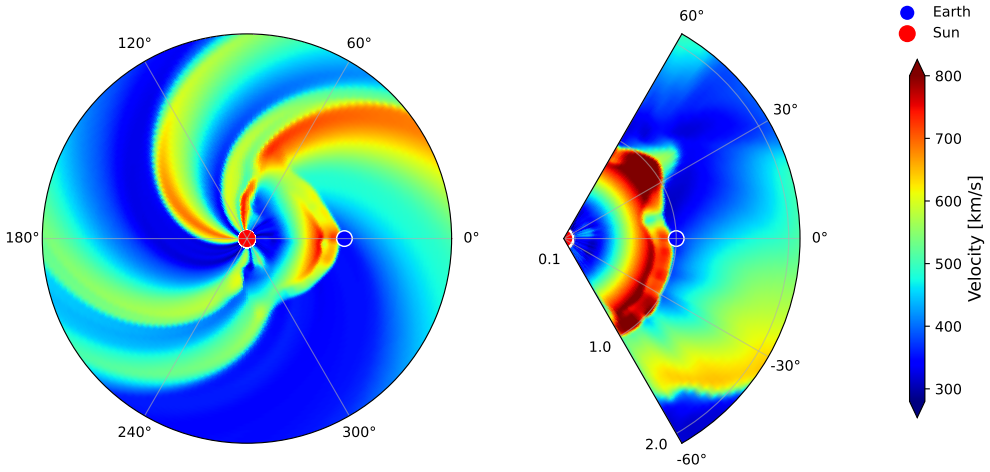

(a2) FR speed (km/s)

Figure 5.5: Solar wind speed snapshot from MHD simulation results for CR 2289 CME 1. (a1) shows the Cone model and (a2) the Flux Rope model.

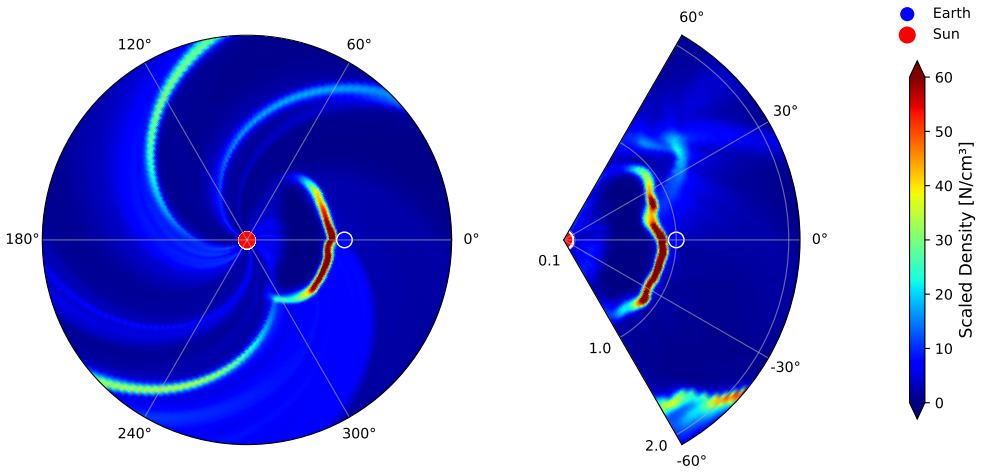

(b1) CONE scaled density (N/cm)

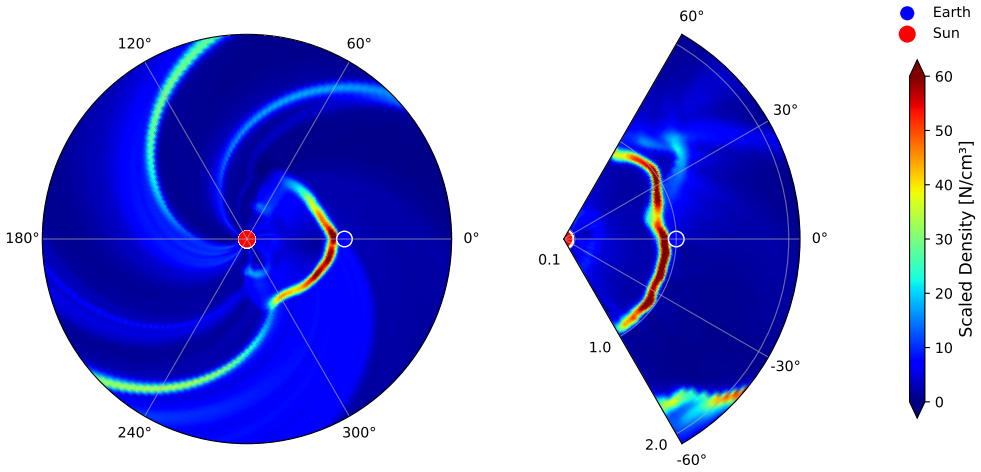

(b2) FR scaled density (N/cm)

Figure 5.6: Scaled density snapshot from MHD simulation results for CR 2289 CME 1. (b1) shows the Cone model and (b2) the Flux Rope model.

CME1 is characterized by relatively weaker physical parameters compared to CME2, with an initial propagation speed of 863 km/s. Once it entered the simulation domain, CME1 did not encounter any strong SIR, and its propagation occurred within a background of slow-speed solar wind. This absence of significant interaction with high-speed solar wind streams allowed CME1 to expand relatively undisturbed as it traversed the inner heliosphere. As CME1 moved outward from the Sun, it displaced the surrounding solar wind plasma, thereby causing a lower-density region in the interplanetary medium along its path. This rarefied region, created in the wake of CME1, had a direct influence on the propagation characteristics of CME2.

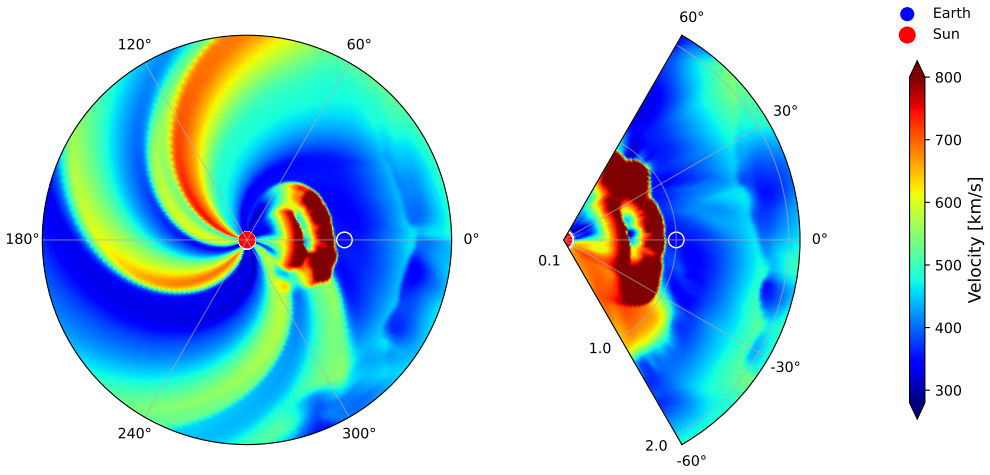

(a1) CONE speed (km/s)

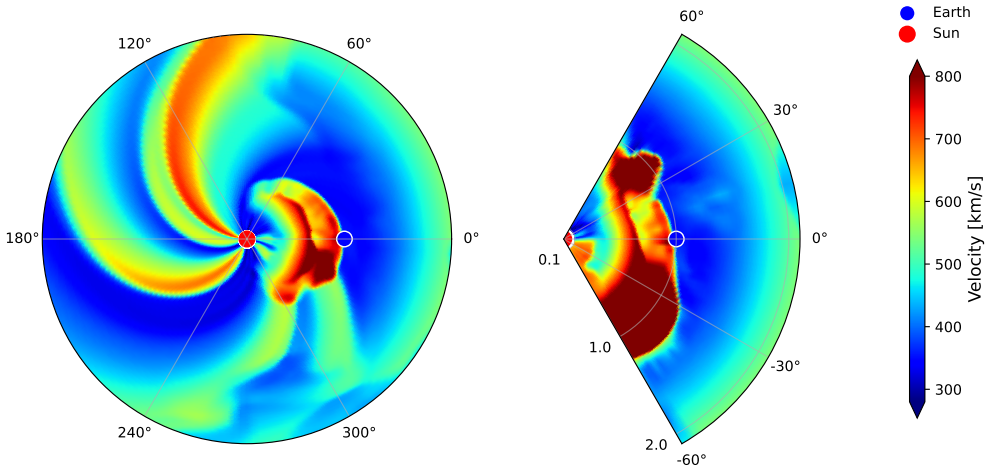

(a2) FR speed (km/s)

Figure 5.7: Snapshot of solar wind speed from MHD simulation results for CR 2289 CME 2. (a1) CONE model and (a2) Flux Rope model.

As CME2 followed the trajectory of CME1, it encountered this preconditioned, less-dense medium because of the absence of SIR or any other geomagnetic storm before the propagation of CME2. The reduced ambient density in the path cleared by CME1 resulted in decreased drag acting on CME2. Consequently, CME2 experienced more efficient outward propagation, with less resistance from the solar wind environment. In the flux rope modeling shown in Figure 5.7, CME2 is observed to interact with two SIR along the path of CME. Although clear signatures of this interaction are not evident in the $r-\phi$ plane, they become more apparent in the $r-\theta$ plane. As a result of this interaction, the western flank of CME2 underwent significant expansion. This expansion was accompanied by a noticeable deflection of the flank, steering it away from the Earth-directed path and towards the direction of the SIR.

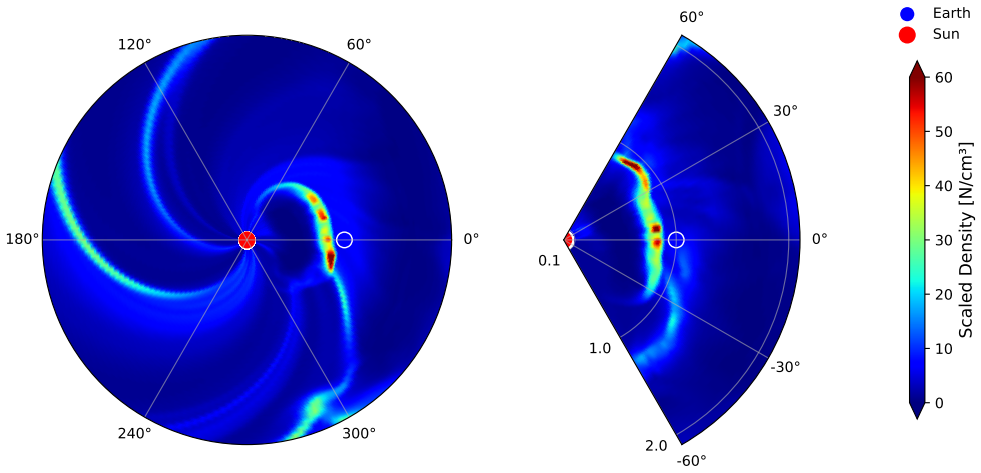

(b1) CONE scaled density (N/cm)

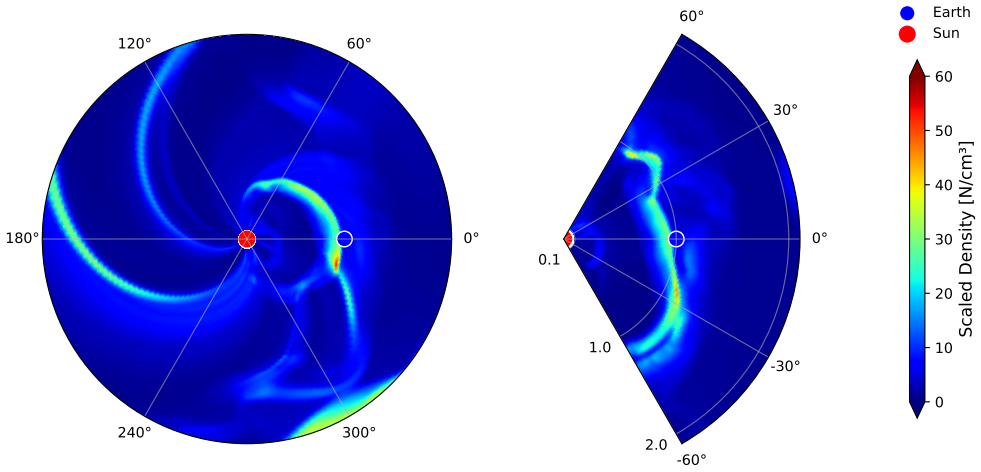

(b2) FR scaled density (N/cm)

Figure 5.8: Snapshot of scaled solar wind density from MHD simulation results for CR 2289 CME 2. (b1) CONE model and (b2) Flux Rope model.

5.2.1 Validation with in situ Measurements

Figure 5.9 illustrates the comparison between the observed and modeled solar wind parameters (speed, proton density, and magnetic field magnitude) at L1 for Carrington Rotation (CR) 2289. The analysis considers two major CMEs. The highlighted regions in the figure correspond to the estimated CME arrival windows.

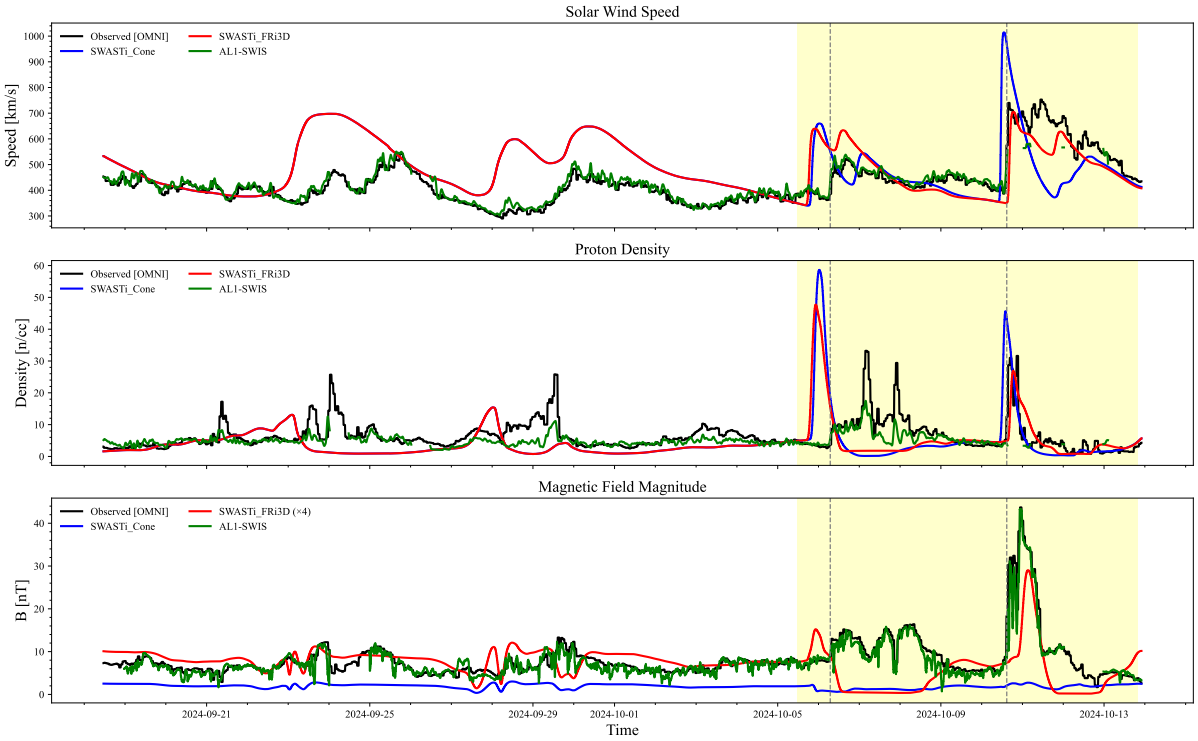

Figure 5.9: Time-series Plot of In Situ Measurements at 1 AU for CR 2289: Simulated Results for FR and Cone CMEs (Blue and Red), Aditya L1 Observed Data (Green), and OMNI Observed Data (Black). Vertical Dashed Lines Mark CME Arrival Time at Earth, with the Shaded Region Indicating CME Simulated. All Data is 1-Hour Moving Average.

Time-series Plot of In Situ Measurements at 1 AU for CR 2289: Simulated Results for FR and Cone CMEs (Blue and Red), Aditya L1 Observed Data (Green), and OMNI Observed Data (Black). Vertical Dashed Lines Mark CME Arrival Time at Earth, with the Shaded Region Indicating CME Simulated. All Data is 1-Hour Moving Average. For the first CME event (CME1), the Cone model exhibited an arrival time error of -6.5 hours, indicating that the predicted shock arrival was 6.5 hours earlier than the observed time. The FR model showed an even earlier arrival, with a prediction error of -9.0 hours. This suggests that while both models anticipated the event in advance of the actual arrival, the Cone model's prediction was closer to the observed timing. In contrast, for the second CME event (CME2), the Cone model forecasted the CME arrival 1.68 hours earlier than observed (-1.68 hours delay), while the FRi3D model predicted the arrival 3.82 hours later than observed (+3.82 hours delay). Overall, this comparison highlights

that the Cone model consistently delivered a more accurate prediction of CME arrival times at L1 for both events.

The FR model demonstrated superior performance in predicting solar wind speed when compared to the cone model. Specifically, the FR model achieved a higher CC of 0.87, compared to 0.33 for the Cone model. This indicates a stronger temporal agreement between the FR model's predictions and the observed data. Moreover, the FR model also produced a significantly lower RMSE of 69.1 km/s, in contrast to 140.5 km/s for the Cone model. Both models struggled to capture the observed variability accurately when analyzing the proton density, as reflected in the generally weaker correlation coefficients. Nonetheless, the FR model consistently demonstrated a relative advantage. The FR model yielded a CC of 0.38, while the Cone model only reached 0.36, indicating poor temporal alignment. Additionally, the RMSE was lower for the FR model, 6.63 N/cc compared to 8.11 N/cc for the Cone model, suggesting that although the correlation was low, the Cone model provided a closer approximation of the density values overall. The complete set of statistical values is provided in Table 5.1. Overall, while the Cone model demonstrated closer arrival times, the Flux Rope (FR) model provided significantly more accurate estimations of the solar wind parameters, particularly for speed and density, as reflected by better CC and RMSE metrics.

Table 5.2: Statistical Comparison of CME Models for CR 2289 Based on 1-Hour Moving Average Values of Speed and Density Against ACE Observations

	Speed Metrics				**Density Metrics**			
Model	**CC**	**RMSE**	**STD**	**Σ**	**CC**	**RMSE**	**STD**	**Σ**
Cone Model	0.332	140.52	0.191	2.458	0.361	8.11	1.452	2.523
FR Model	0.873	69.19	0.125	0.510	0.382	6.63	1.179	1.775

5.3 Result: CR 2290

In this event, we simulated two CMEs. CME1 was initiated on 2024-10-26 at 06:48 UT and entered the simulation domain at 08:52 UT. Snapshots of the evolution of CME1 speed and sclaed density are shown in Figure 5.10 and Figure 5.11 and CME2 are shown in Figure 5.12 and Figure 5.13.

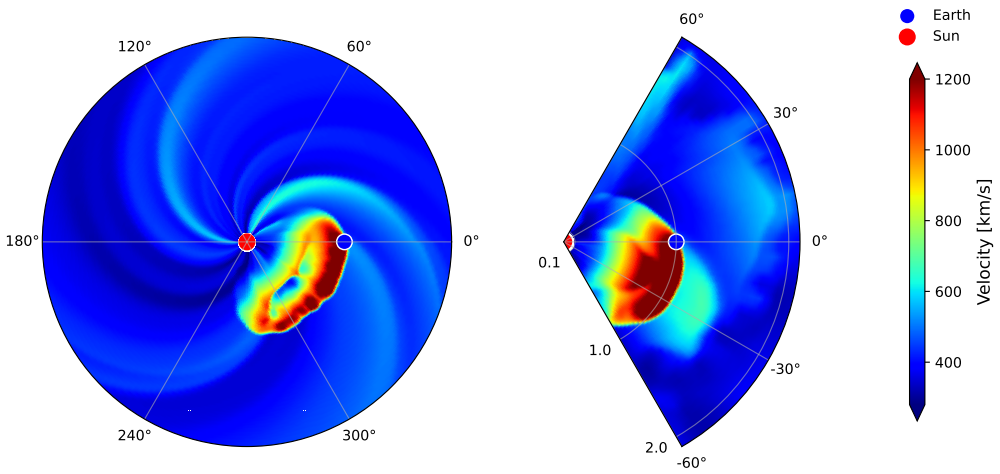

(a1) CONE speed (km/s)

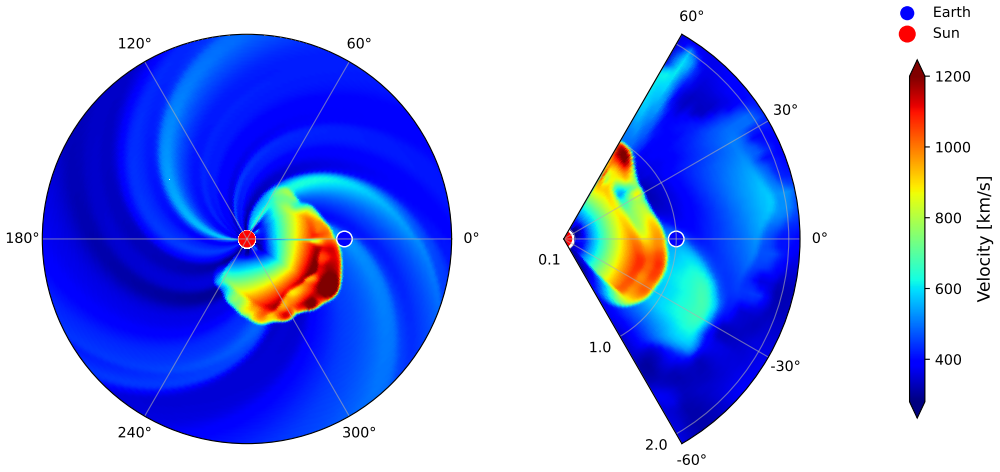

(a2) FR speed (km/s)

Figure 5.10: Snapshot of solar wind speed from MHD simulation results for CR 2290 CME 1. (a1) CONE model and (a2) Flux Rope model.

As illustrated in Figure 5.10 and Figure 5.11, the CME1 eruption originated from a latitude of $-19°$ and a longitude of $-34°$, with a half-width and half-height of 54°. CME2 originated at a latitude of $-21°$ and a longitude of 33°, with a half-width of 52°. As we can see from the initial plot, there was no powerful SIR. However, the eastern flank of the CME propagated close to the weak SIR. Despite the CME1 speed of 1677 km/s, it

did not follow the stream. From the r–θ FR and cone model plot, it is evident that the SIR is passing through Earth's position. Therefore, before the CME reaches Earth's location, it encounters a high-density region, which causes drag on the CME as well. CME2 propagated into a comparatively high-speed solar wind background. In the FR model, it is evident that the eastern edge of the CME2 is connected to the SIR. As the CME continues to propagate, the eastern flank expands further. However, CME2 results in only a glancing blow to Earth.

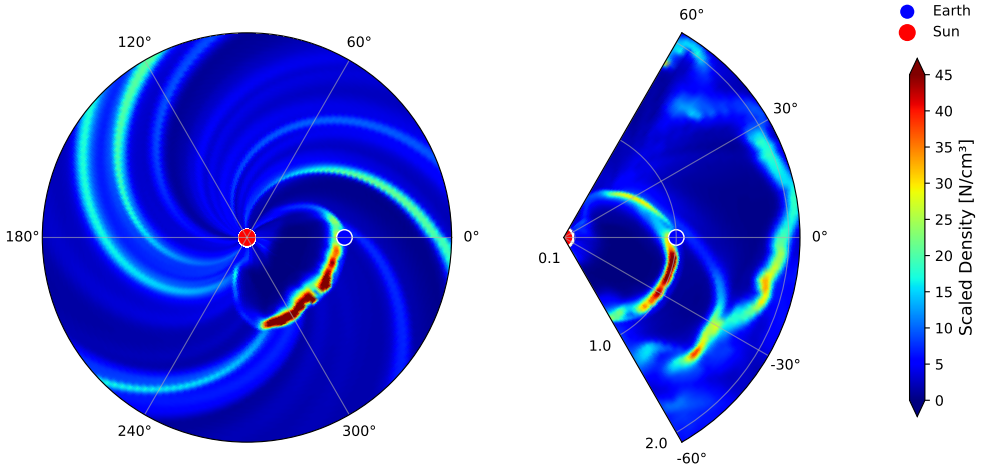

(b1) CONE scaled density (N/cm)

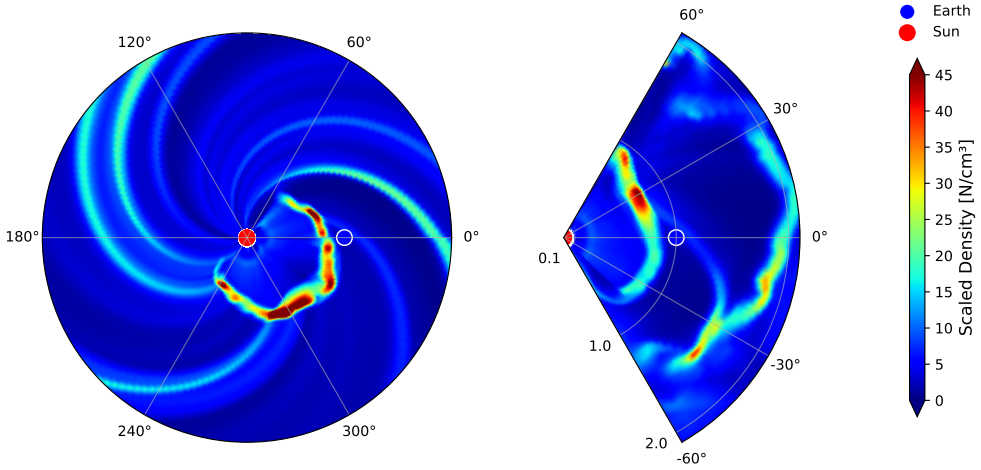

(b2) FR scaled density (N/cm)

Figure 5.11: Snapshot of scaled solar wind density from MHD simulation results for CR 2290 CME 1. (b1) CONE model and (b2) Flux Rope model.

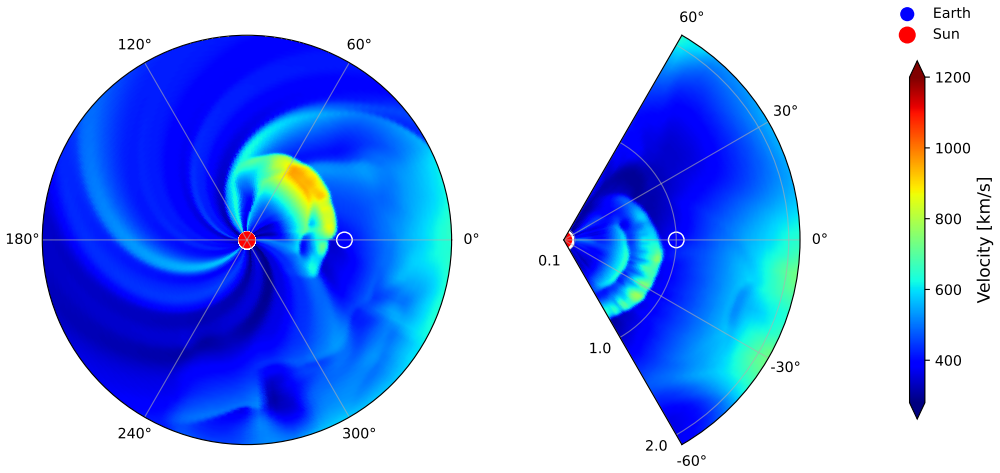

(a1) CONE speed (km/s)

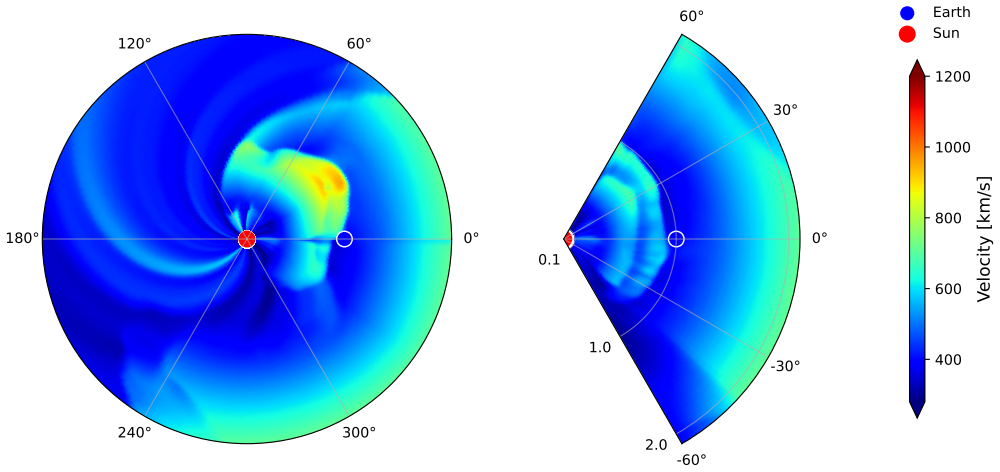

(a2) FR speed (km/s)

Figure 5.12: Snapshot of solar wind speed from MHD simulation results for CR 2290 CME 2. (a1) CONE model and (a2) Flux Rope model.

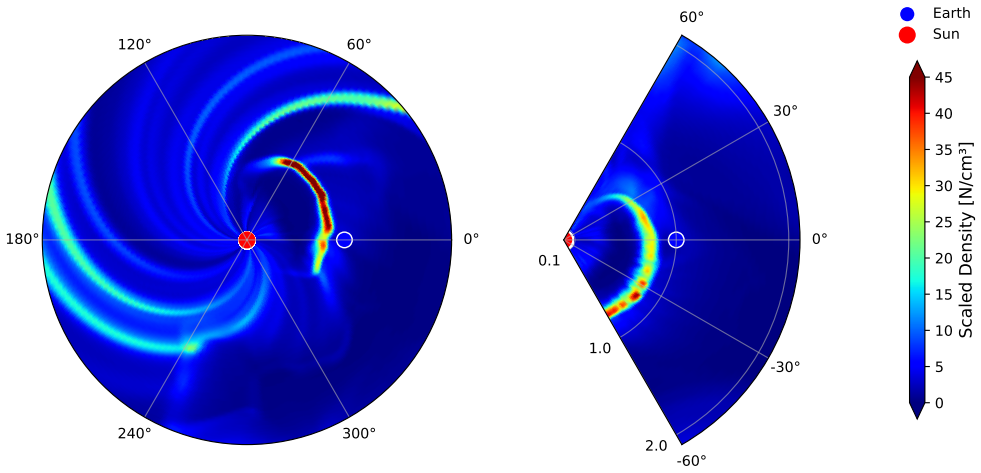

(b1) CONE scaled density (N/cm)

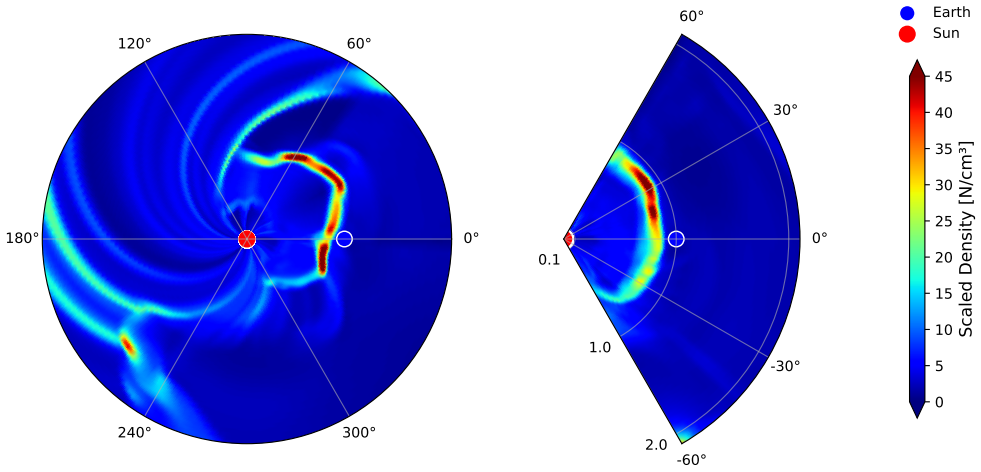

(b2) FR scaled density (N/cm)

Figure 5.13: Snapshot of scaled solar wind density from MHD simulation results for CR 2290 CME 2. (b1) CONE model and (b2) Flux Rope model.

5.3.1 Validation with in situ Measurements

Figure 5.14 presents the comparison between the observed and modeled solar wind parameters (speed, proton density) at L1 for Carrington Rotation (CR) 2290. The analysis includes two major CME events. The highlighted regions in the figure correspond to the estimated CME arrival windows.

For the first CME event (CME1), the Cone model predicted an arrival time with a delay of +9.8 hours, indicating that the shock was forecasted to arrive 9.8 hours later than the observed time. The FR model, on the other hand, predicted an even later arrival, with a delay of +14.37 hours. This suggests that both models overestimated the arrival time, with the Cone model's prediction being closer to the observed time. For the

second CME event (CME2), the Cone model predicted an arrival time with a delay of +24.20 hours, while the FR model forecasted the arrival +28.03 hours later than observed. Once again, both models exhibited an overestimation in arrival timing, with the Cone model's prediction being somewhat more accurate compared to the FR model. Overall, this comparison indicates that while both models struggled with accurately predicting the arrival time of the CMEs, the Cone model provided a more timely prediction for both events.

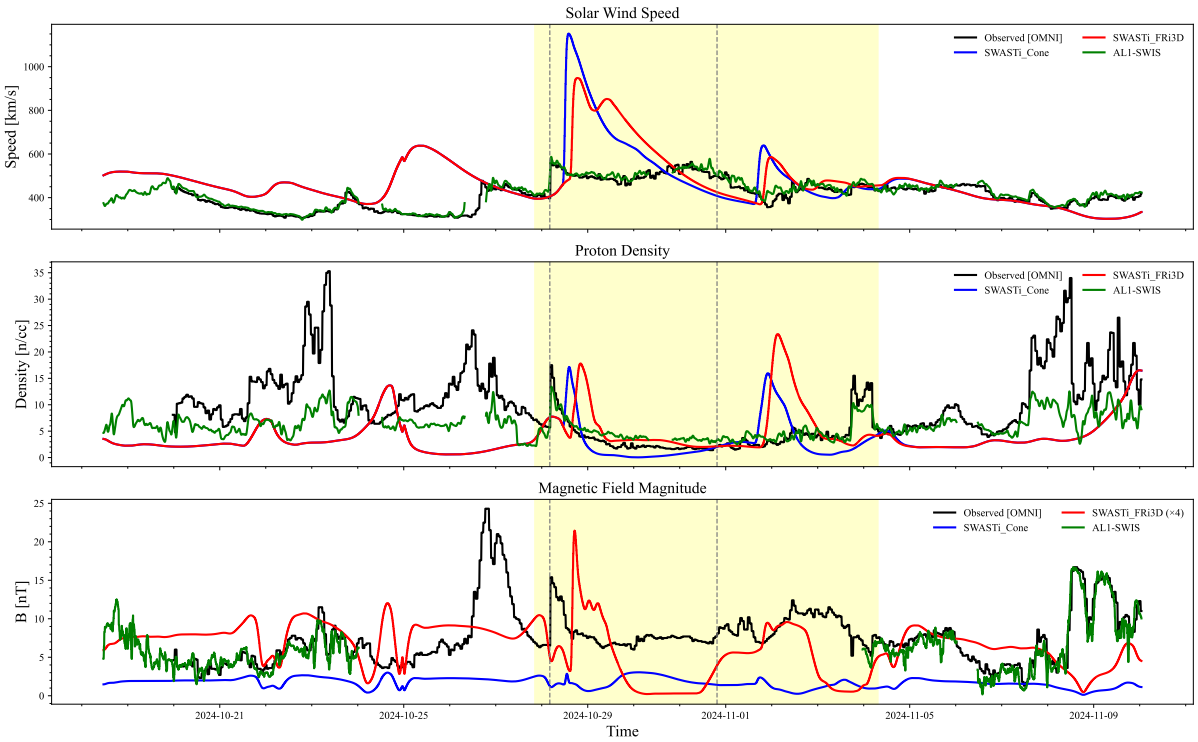

Figure 5.14: Time-series Plot of In Situ Measurements at 1 AU for CR 2290: Simulated Results for FR and Cone CMEs (Blue and Red), Aditya L1 Observed Data (Green), and OMNI Observed Data (Black). Vertical Dashed Lines Mark CME Arrival Time at Earth, with the Shaded Region Indicating CME Simulated. All Data is 1-Hour Moving Average.

When analyzing solar wind speed, the Cone model exhibited a relatively weak correlation with the observed data, with a CC of 0.48, and an RMSE of 138 km/s. This suggests that the Cone model's predictions had a moderate temporal agreement with the observed values but were relatively inaccurate in terms of magnitude. In contrast, the FR model showed a improved performance, with a CC of 0.55 and an RMSE of 122 km/s. Although the FR model exhibits a higher CC, it also presents lower error values compared to the Cone model. Based on the Σ value, the Cone model demonstrates better overall alignment with the observed data. For proton density, Cone model showed a good performance in capturing the observed variability. The Cone model had a CC of 0.32 and an RMSE of 4.28 N/cc, while the FR model showed a weaker CC of 0.12 but a

slightly higher RMSE of 4.9 N/cc. The Cone model is slightly better at approximating the density values than the FR model.

Table 5.3: Statistical Comparison of CME Models for CR 2290 Based on 1-Hour Moving Average Values of Speed and Density Against Aditya-L1 Observations

	Speed Metrics				Density Metrics			
Model	**CC**	**RMSE**	**STD**	**Σ**	**CC**	**RMSE**	**STD**	**Σ**
Cone Model	0.488	138.11	0.529	2.449	0.327	4.282	0.350	0.577
FR Model	0.551	122.26	0.490	1.937	0.129	4.993	0.437	0.952

5.4 Forecasting with the pipeline

As part of the pipeline demonstration, a forward simulation was conducted for a recent dates event for which in-situ observational data is not yet available. While validation is pending due to the lack of spacecraft measurements at the time of writing, the simulation provides a valuable preview of the CME's potential propagation characteristics and its interaction with the ambient solar wind.

For the forecasting demonstration, we conducted a simulation covering the period from 2025-03-30 UT to 2025-04-24 UT. During this time window, no major CME events with significant impacts were recorded. Only a few minor CMEs were observed, most of which were weak and resulted in negligible or glancing interactions with Earth's magnetosphere. Therefore, in this particular simulation run, no CMEs were explicitly included, and the focus was placed solely on modeling the background solar wind conditions. As illustrated in Figure 5.15, the simulated solar wind during this period exhibits a reasonable level of agreement with the available in-situ measurements, particularly in regions where data overlap exists. Although minor discrepancies are expected due to the avoidance of the CMEs present.

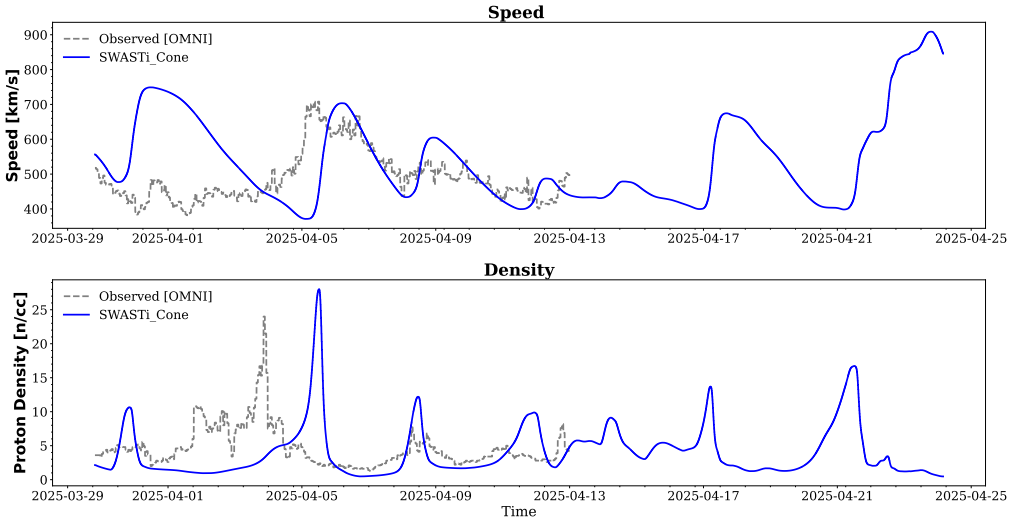

Figure 5.15: Time-series plot of in-situ measurements at 1 AU for the forecasting period from 2025-03-30 UT to 2025-04-24 UT. Simulated results from the pipeline are shown in blue, while in-situ ACE data are represented by grey dotted lines.

The modular structure of the pipeline allows it to adapt to different forecasting time-frames . Depending on the frequency and availability of input magnetograms, the system can be configured for daily, weekly, or monthly space weather forecasts. This flexibility makes it suitable for both operational monitoring and long-term planning scenarios. As new in-situ data becomes available, the forecasts generated by the pipeline can be retrospectively validated and refined, further enhancing the model's reliability and performance. This forecasting fall within Carrington Rotation CR 2296, and we plan to continue the simulation for the CR 2297 subsequent rotations to extend the forecast and further evaluate the pipeline's long-term performance.

Chapter 6

Conclusions and Future Directions

This thesis focused on the development and implementation of a comprehensive, automated pipeline for Coronal Mass Ejection (CME) simulation as part of the broader effort to improve space weather modeling and forecasting. The work was carried out in two major phases: (1) the design and realization of the automated CME simulation pipeline, and (2) the application of this system for simulating specific CME events and evaluating its performance in a real-world context.

Space Weather Pipeline Development: The first phase of the thesis was dedicated to building the architecture for the automated pipeline. The pipeline was designed to automate all the process, including the heliospheric module and inner heliospheric module. Key components of the system included automated data acquisition, parameter preprocessing, modular simulation stages, and post-simulation analysis tools. The architecture was built with a high degree of automation and containerization, ensuring portability and reproducibility across different computational environments. Docker-based modules were utilized to compartmentalize the different stages of the simulation workflow, enabling seamless integration of various models, including the WSA model for coronal background solar wind, the HUX model for heliospheric evolution, and the PLUTO MHD code for advanced inner heliospheric simulations. The pipeline was architected with scalability and flexibility in mind, serving as a robust platform that can readily incorporate future advancements in CME modeling or integrate additional observational inputs. To ensure broad accessibility and ease of deployment, the entire system was containerized with all necessary dependencies bundled within the Docker environment. This design eliminates the need for users to alter or configure their host operating systems, ensuring platform independence and minimal setup complexity. Furthermore, the pipeline supports parallel processing, significantly enhancing simulation efficiency and performance, while improving user experience through faster execution times and improved resource utilization. This

part of the work not only provided a reusable framework for space weather simulations but also contributed to the effort of operationalizing research-grade models for practical forecasting applications. Moreover, the modular and containerized design of the pipeline allows for seamless integration with cloud-based computing platforms. This capability enables researchers and operational users to deploy and run simulations on scalable cloud infrastructure, facilitating rapid and efficient space weather modeling. Such flexibility is crucial for timely forecasting, improved situational awareness, and mitigation of space weather impacts on critical technologies and infrastructure.

Event Simulation and Validation: In the second phase, the developed pipeline was applied to the simulation of real CME events. A series of case studies were carried out, including events during solar minima, to test the pipeline's ability to reproduce observational features and match in-situ measurements. Through these simulations, key CME parameters such as propagation speed, arrival time, and solar wind structure were extracted and compared against observed data.

For the detailed CME event simulations presented in Chapter 5, we selected Carrington Rotations (CR) 2288, 2289, and 2290. These events were simulated using both the CONE model which is integrated within the developed pipeline—and a standalone flux rope model (SWASTi FRi3D) for comparative analysis. The simulation outputs were evaluated against in-situ solar wind observations from the ADITYA-L1 spacecraft. Notably, the speed and density profiles from the CR 2288 and 2289 simulations exhibited strong correlation with the corresponding in-situ measurements. This agreement highlights the reliability and accuracy of the pipeline, affirming its capability to reproduce realistic solar wind conditions and CME propagation dynamics.

Scientific and Practical Contributions: From a scientific standpoint, the thesis contributes to the growing body of work that bridges solar physics with operational space weather forecasting. By automating and integrating complex simulation stages into a cohesive pipeline, this work addresses a longstanding gap between research tools and real-time applications. The ability to simulate CMEs in a modular, end-to-end fashion opens avenues for ensemble forecasting, uncertainty quantification, and predictive analytics, all of which are critical for the next generation of space weather services.

From a practical perspective, the pipeline offers a scalable and adaptable tool that can be used by researchers, government agencies, and private stakeholders interested in space weather impacts on satellite operations, navigation systems, and ground-based infrastructure. The design choices, particularly the use of containerization and scripting, ensure that the pipeline can be deployed in various environments with minimal manual

configuration, supporting reproducible science.

6.1 Future Directions

This thesis lays the groundwork for several promising future directions.

- A key future direction of this work is the development of an open, end-to-end space weather modeling system that spans from the Sun to the Earth. The vision is to create a flexible and modular environment capable of coupling multiple space weather models hosted locally or distributed across geographically dispersed compute clusters into a unified simulation framework. This integrated approach would enable comprehensive modeling of the entire Sun-Earth system, improving both scientific understanding and forecasting capabilities.

- To further enhance the forecasting capabilities of the pipeline, a Surface Flux Transport (SFT) model can be incorporated to predict the future evolution of active regions and sunspots on the solar surface. By forecasting the magnetic field distribution on the Sun, the SFT model can serve as a forward-looking input generator for CME initiation, enabling the pipeline to anticipate space weather events before they occur. Automating this input process would significantly advance the system, transitioning it from a reactive simulation tool to a predictive forecasting framework capable of real-time space weather modeling.

- Another is the expansion of the pipeline to include CME-CME interaction modeling, which will help to make the simulation better.

In conclusion, this thesis delivers a fully functional, automated simulation system for solar wind and CMEs and validates its application through detailed event simulations. It contributes not only to the advancement of solar-terrestrial research but also to the operational readiness of next-generation space weather forecasting systems. The framework developed here represents a meaningful step toward closing the gap between academic modeling efforts and practical forecasting tools needed to mitigate the risks posed by solar activity in an increasingly technology-reliant world.

Bibliography

Martin D Altschuler and Gordon Newkirk. Magnetic fields and the structure of the solar corona: I: Methods of calculating coronal fields. *Solar Physics*, 9:131–149, 1969.

Odstrčil D Arge, CN, VJ Pizzo, and LR Mayer. Aip conf. proc. 679, solar wind ten. *AIP*, 2003.

E. Echer, W.D. Gonzalez, F.L. Guarnieri, A. Dal Lago, and L.E.A. Vieira. Introduction to space weather. *Advances in Space Research*, 35(5):855–865, 2005. ISSN 0273-1177. doi: https://doi.org/10.1016/j.asr.2005.02.098. URL https://www.sciencedirect.com/science/article/pii/S0273117705004709. Fundamentals of Space Environment Science.

Molly L Goelzer, Nathan A Schwadron, and Charles W Smith. An analysis of alfvén radius based on sunspot number from 1749 to today. *Journal of Geophysical Research: Space Physics*, 119(1):115–120, 2014.

N. Gopalswamy. *A Global Picture of CMEs in the Inner Heliosphere*, pages 201–251. Springer Netherlands, Dordrecht, 2004. URL https://doi.org/10.1007/978-1-4020-2831-1_8.

Alexey Isavnin. Fried: A novel three-dimensional model of coronal mass ejections. *The Astrophysical Journal*, 833(2):267, 2016.

Justin Christophe Kasper. *Solar wind plasma: kinetic properties and micro-instabilities*. PhD thesis, Massachusetts Institute of Technology, 2002.

Olga E. Malandraki and Norma B. Crosby. *Solar Energetic Particles and Space Weather: Science and Applications*, pages 1–26. Springer International Publishing, Cham, 2018. doi: 10.1007/978-3-319-60051-2_1. URL https://doi.org/10.1007/978-3-319-60051-2_1.

Prateek Mayank, Bhargav Vaidya, and D Chakrabarty. Swasti-sw: space weather adaptive simulation framework for solar wind and its relevance to the aditya-l1 mission. *The Astrophysical Journal Supplement Series*, 262(1):23, 2022. doi: 10.3847/1538-4365/ac8551. URL https://iopscience.iop.org/article/10.3847/1538-4365/ac8551.

Prateek Mayank, Bhargav Vaidya, Wageesh Mishra, and D Chakrabarty. Swasti-cme: A physics-based model to study coronal mass ejection evolution and its interaction with solar wind. *The Astrophysical Journal Supplement Series*, 270(1):10, 2023. doi: 10.3847/1538-4365/ad08c7. URL https://iopscience.iop.org/article/10.3847/1538-4365/ad08c7.

S. L. McGregor, W. J. Hughes, C. N. Arge, M. J. Owens, and D. Odstrcil. The distribution of solar wind speeds during solar minimum: Calibration for numerical solar wind modeling constraints on the source of the slow solar wind. *Journal of Geophysical Research: Space Physics*, 116(A3), 2011. doi: https://doi.org/10.1029/2010JA015881. URL https://agupubs.onlinelibrary.wiley.com/doi/abs/10.1029/2010JA015881.

Andrea Mignone, G Bodo, S Massaglia, Titos Matsakos, O ea Tesileanu, C Zanni, and Anthony Ferrari. Pluto: a numerical code for computational astrophysics. *The Astrophysical Journal Supplement Series*, 170(1):228, 2007.

D Odstrcil. Modeling 3-d solar wind structure. *Advances in Space Research*, 32(4): 497–506, 2003.

Jens Pomoell and Stefaan Poedts. Euhforia: European heliospheric forecasting information asset. *Journal of Space Weather and Space Climate*, 8:A35, 2018.

Pete Riley and Opal Issan. Using a heliospheric upwinding extrapolation technique to magnetically connect different regions of the heliosphere. *Frontiers in Physics*, 9: 679497, 2021.

Kenneth H Schatten. Current sheet magnetic model for the solar corona. Technical report, 1971.

D Shiota, R Kataoka, Y Miyoshi, T Hara, C Tao, K Masunaga, Y Futaana, and N Terada. Inner heliosphere mhd modeling system applicable to space weather forecasting for the other planets. *Space Weather*, 12(4):187–204, 2014.

David Stansby, Anthony Yeates, and Samuel Badman. pfsspy: A python package for potential field source surface modelling. *Journal of Open Source Software*, 5(54), 2020.

Gábor Tóth, Igor V Sokolov, Tamas I Gombosi, David R Chesney, C Robert Clauer, Darren L De Zeeuw, Kenneth C Hansen, Kevin J Kane, Ward B Manchester, Robert C Oehmke, et al. Space weather modeling framework: A new tool for the space science community. *Journal of Geophysical Research: Space Physics*, 110(A12), 2005.

Reka M Winslow, Camilla Scolini, Noé Lugaz, and Antoinette B Galvin. The effect of stream interaction regions on icme structures observed in longitudinal conjunction. *The Astrophysical Journal*, 916(1):40, 2021.

S. Yashiro, Sachiko Akiyama, Nat Gopalswamy, and Russell A. Howard. Different power-law indices in the frequency distributions of flares with and without coronal mass ejections. *The Astrophysical Journal Letters*, 650:L143 – L146, 2006. URL https://api.semanticscholar.org/CorpusID:6406382.